Motion Detection in Diffraction Tomography by Common Circle Methods

Michael Quellmalz* Peter Elbau† Otmar Scherzer†‡§ Gabriele Steidl*

May 8, 2023

Abstract

The method of common lines is a well-established reconstruction technique in cryogenic electron microscopy (cryo-EM), which can be used to extract the relative orientations of an object given tomographic projection images from different directions.

In this paper, we deal with an analogous problem in optical diffraction tomography. Based on the Fourier diffraction theorem, we show that rigid motions of the object, i.e., rotations and translations, can be determined by detecting common circles in the Fourier-transformed data. We introduce two methods to identify common circles. The first one is motivated by the common line approach for projection images and detects the relative orientation by parameterizing the common circles in the two images. The second one assumes a smooth motion over time and calculates the angular velocity of the rotational motion via an infinitesimal version of the common circle method. Interestingly, using the stereographic projection, both methods can be reformulated as common line methods, but these lines are, in contrast to those used in cryo-EM, not confined to pass through the origin and allow for a full reconstruction of the relative orientations. Numerical proof-of-the-concept examples demonstrate the performance of our reconstruction methods.

Keywords. Diffraction tomography, motion detection, Fourier diffraction theorem, common circle method, optical imaging.

Math Subject Classifications. 92C55, 78A46, 94A08, 42B05.

1 Introduction

A key task in many imaging modalities consists in recovering an object's inner structure given images of its illuminations from different directions. The *X-ray computed tomography* (CT) is based on a number of assumptions, most prominently that the light travels along straight lines. If, however, the object is small compared to the wavelength of the illumination, the optical diffraction cannot be neglected anymore. This occurs for example when examining structures with a size of a few micrometers such as biological cells with visible light. In the so-called *optical diffraction tomography*, we respect the wave character of the light and take optical diffraction into account.

*TU Berlin, Straße des 17. Juni 136, D-10587 Berlin, Germany, {quellmalz, steidl}@math.tu-berlin.de.

†University of Vienna, Oskar-Morgenstern-Platz 1, A-1090 Vienna, Austria, {otmar.scherzer, peter.elbau}@univie.ac.at

‡Johann Radon Institute for Computational and Applied Mathematics (RICAM), Altenbergerstraße 69. A-4040 Linz, Austria

§Christian Doppler Laboratory for Mathematical Modeling and Simulation of Next Generations of Ultrasound Devices (MaMSi), Oskar-Morgenstern-Platz 1, A-1090 Vienna, Austria

As biological samples should be imaged preferably in a natural environment, contact-free manipulation methods are used for rotating the object during the image acquisition process. Such rotations can be induced by optical [15] or acoustical tweezers [7, 23, 34].

Therefore, additional effort is necessary if the rigid motion of the object during the image acquisition process is unknown and has to be reconstructed from the captured images. In this paper, we propose to tackle this problem by a method of common circles and its infinitesimal version which is inspired by the well-known method of common lines for projection images as applied in cryogenic electron microscopy (cryo-EM) [32, 35, 37]. Let us briefly recall this method first.

Method of common lines. In computed tomography, the aim is the reconstruction of an object from given (optical) projection images for different directions of the imaging wave or, equivalently, different rotations of the object. The object's absorption properties are described by a function $f\colon \mathbb{R}^3 \to \mathbb{R}$, which has to be recovered. We assume the object moves in time t according to rotation matrices R_t, and the illumination is in direction $\boldsymbol{e}^3 = (0,0,1)^\top$. Then, the *ray transform* of f is given by

$$\mathcal{X}_{R_t}[f](x_1,x_2) \coloneqq \int_{-\infty}^{\infty} f\left(R_t\,(x_1,x_2,x_3)^\top\right)\,\mathrm{d}x_3, \qquad (x_1,x_2)^\top \in \mathbb{R}^2. \tag{1.1}$$

The reconstruction of f is based on the Fourier slice theorem, see e.g. [28, Theorem 2.11], which states that

$$\mathcal{F}^{(2)}[\mathcal{X}_{R_t}[f]](k_1,k_2) = \sqrt{2\pi}\,\mathcal{F}^{(3)}[f](R_t\,(k_1,k_2,0)^\top), \qquad (k_1,k_2)^\top \in \mathbb{R}^2, \tag{1.2}$$

where $\mathcal{F}^{(2)}$ and $\mathcal{F}^{(3)}$ denote the two- and three-dimensional Fourier transforms, see (2.6). Hence, given the data $\mathcal{X}_{R_t}[f]$ for the rotation R_t, we obtain the Fourier transform of f on the plane $P_{R_t} \coloneqq \{R_t\,(k_1,k_2,0)^\top : (k_1,k_2)^\top \in \mathbb{R}^2\}$ through the origin. If the rotations R_t are known and the planes P_{R_t} fully cover $\mathbb{R}^3$, e.g. when the object makes a full turn around a fixed rotation axis other than $\boldsymbol{e}^3$, then we can reconstruct f by the inverse 3D Fourier transform. However, in cryo-EM, the rotations R_t of the object are not known. The method of common lines makes use of the fact that two planes P_{R_s} and P_{R_t} intersect for $R_s\boldsymbol{e}^3 \neq \pm R_t\boldsymbol{e}^3$ in a common line which contains the origin. This common line can be detected from the projection data $\mathcal{X}_{R_s}$ and $\mathcal{X}_{R_t}$ by maximizing the correlation of all possible combinations of lines in the two planes, which is a minimization problem in two variables. Note that the common line detection is usually not performed directly in the Fourier space, but by comparing lines of the 2D Radon transform of $\mathcal{X}_{R_t}[f]$, see [36] and also [3] for computational methods. Keeping one plane fixed, the second plane is not uniquely determined just by their common line, see Figure 1 (left side). We have to compute the pairwise common lines between three planes to determine the rotation angles between them, see Figure 1 (right side). Alternatively, the reconstruction can be done by moment-based methods [20]. Furthermore, Kam's method considers reconstructing f without the need of computing the motion parameters first [17, 31].

Diffraction tomography. In optical diffraction tomography, we use a modeling based on Born's or Rytov's approximation of the scattered wave, see e.g. [16, Chapter 6]. The Fourier diffraction theorem [38] provides a relation between the measured and Fourier-transformed data and the Fourier transform of the scattering potential, which we want to reconstruct conceptually similar as for the method of common lines in (1.2). Once we know the motion parameters, the scattering potential can be reconstructed using a backpropagation formula [6, 27] or inverse discrete Fourier methods [21], which can deal with arbitrary, irregular motions. Under Born's approximation and certain conditions on the moments of the scattering potential, it was shown [22] that there exists a unique solution to the problem of determining the scattering potential

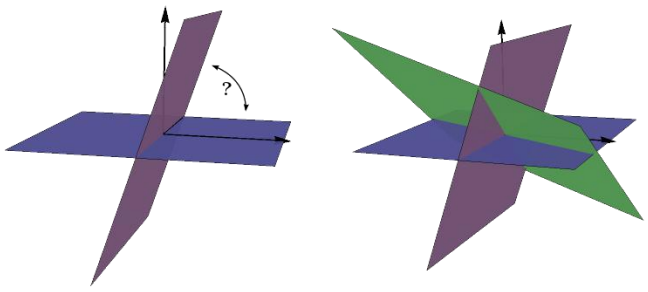

Figure 1: *Left:* A common line pair between two planes P_{R_s} and P_{R_t} does not determine the relative angle between them uniquely. *Right:* Knowing pairwise common lines between three planes, we can determine their orientations uniquely (except for degenerate cases). Courtesy of Denise Schmutz from [30, Figure 6.2 and Figure 6.3].

given measurements with unknown object rotations in an experiment where all possible rotations of the object are performed.

In this paper, we are interested in an experimental setup where the parameters of the rigid motion need to be determined in parallel to the tomographic reconstruction. We show that the rotations can be determined by an approach which we call the "method of common circles". It is based on computing a common circular arc of intersecting hemispheres. In particular, we show that only two hemispheres are required to compute the rotation, whereas, in the context the inversion of the ray transform based on the Fourier slice theorem, one needs to consider the intersection of three planes. Furthermore, the object's translation can be completely determined from the measurement data under some assumptions on the object. This is in contrast to the ray transform, where the measurements are invariant to every translation of the object in direction of the incident wave. The diffraction data is sensitive to the third component of the translations, which allows the full recovery. The concept of common circles or common arcs was addressed in an empirical way in [13], and its application for recovering rotations in the context of crystallography was sketched in [4]. In this paper, we give a rigorous mathematical treatment of the motion reconstruction, which includes also the determination of translations of the object and an approach based on a time-continuous motion. For instance, time-continuous motions are appropriate to model tomographic experiments where the object is moved with tweezers. In these experiments the motion is continuous but not uniform as in medical CT. Such models are in general simpler than Cyro-tomographic experiments, where in a pre-processing steps X-ray projection images need to be aligned (numbered) according to their orientations. In this sense tomographic reconstructions based on a time-continuous movement are simpler than standard Cryo-tomographic problems. Moreover, when we assume a time-continuous rigid movement, we can use an infinitesimal calculus for deriving reconstruction methods, leading to the method of *infinitesimal common circle* motion estimation (see Section 4).

Outline of this paper. In Section 2, we describe the model of diffraction tomography with the object undergoing a rigid motion. Then, in Section 3, we derive the common circle method for reconstructing the object's *rotations*. In Section 4, we give an infinitesimal version of the common circle method, where we assume that the rotations depend smoothly on the time. Section 5 covers the reconstruction of the *translations* of the object. In Section 6, we describe reconstruction methods based on our theoretical findings. We perform numerical proof-of-concept simulations in Section 7 of the proposed methods with two different phantoms and two different motion experiments. Moreover, based the infinitesimal approach, we can efficiently compute an initialization for our optimization algorithm in the direct common circle method. We postpone

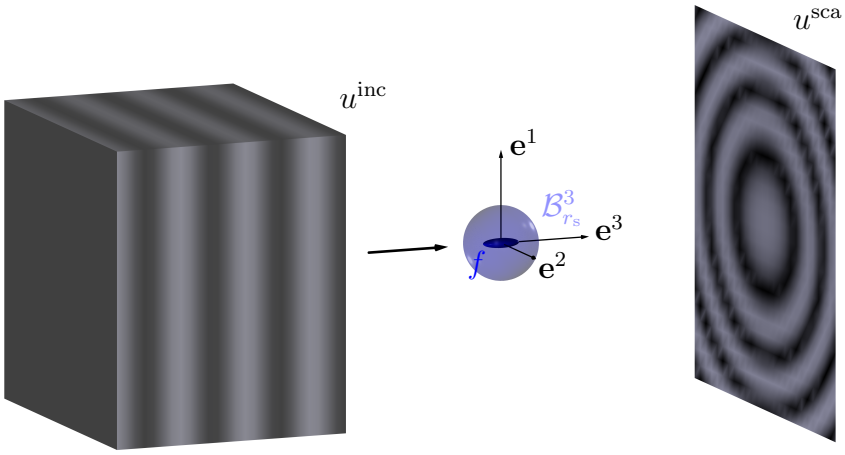

Figure 2: Experimental setup of transmission imaging in optical diffraction tomography.

technical proofs to Appendix A - C. An interesting relation between common circles and common lines based on the stereographic projection is outlined in Appendix D.

2 Diffraction Tomography

2.1 Fourier diffraction theorem

Throughout this paper, we consider the following experimental setup of *optical diffraction tomography*, which is described in detail in [21, 38]. The unknown object is illuminated by an *incoming plane wave*, which propagates in direction $\boldsymbol{e}^3$ with wave number $k_0 > 0$. This is represented by a function

$$u^{\mathrm{inc}}(\boldsymbol{x}) \coloneqq \mathrm{e}^{\mathrm{i}k_0 x_3}, \quad \boldsymbol{x} \in \mathbb{R}^3, \tag{2.1}$$

where we normalized the amplitude to one. The object shall be contained in an open ball $\mathcal{B}^3_{r_s}$ of some radius $r_s > 0$, where we use the notation

$$\mathcal{B}^d_r \coloneqq \{\boldsymbol{x} \in \mathbb{R}^d : \|\boldsymbol{x}\| < r\} \quad \text{for } d \in \mathbb{N},\ r > 0,$$

with the Euclidean norm $\|\cdot\|$. Further, we will need spheres $\partial\mathcal{B}^d_r(\boldsymbol{z}) \coloneqq \{\boldsymbol{y} \in \mathbb{R}^d : \|\boldsymbol{y} - \boldsymbol{z}\| = r\}$. Then the incident wave u^{inc} induces a *scattered wave* u^{sca} which is recorded in transmission imaging in a plane $\{\boldsymbol{x} \in \mathbb{R}^3 : x_3 = r_{\mathrm{M}}\}$ at a position $r_{\mathrm{M}} > r_s$ outside the object, see Figure 2. The scattered wave u^{sca} can be calculated from the incoming wave u^{inc} and the *scattering potential* $f\colon \mathbb{R}^3 \to \mathbb{R}_{\geq 0}$, which is a piecewise continuous function with support in $\mathcal{B}^3_{r_s}$, of the unknown object as a solution of the partial differential equation

$$-(\Delta + k_0^2)u^{\mathrm{sca}}(\boldsymbol{x}) = f(\boldsymbol{x})\left(u^{\mathrm{sca}}(\boldsymbol{x}) + u^{\mathrm{inc}}(\boldsymbol{x})\right), \qquad \boldsymbol{x} \in \mathbb{R}^3, \tag{2.2}$$

which fulfills the Sommerfeld radiation condition

$$\lim_{r\to\infty} \max_{\|\boldsymbol{x}\|=r} \|\boldsymbol{x}\| \left|\langle \nabla u^{\mathrm{sca}}(\boldsymbol{x}), \tfrac{\boldsymbol{x}}{\|\boldsymbol{x}\|}\rangle - \mathrm{i}k_0 u^{\mathrm{sca}}(\boldsymbol{x})\right| = 0.$$

The condition that f is real-valued means that no absorption occurs in the object. If $\|f\|_\infty$ is sufficiently small, the solution u^{sca} is small in comparison to u^{inc}, so that it can be neglected on the right-hand side of (2.2) and we obtain the *Born approximation* u of the scattered field u^{sca}, determined by

$$-(\Delta + k_0^2)u = f u^{\mathrm{inc}}, \tag{2.3a}$$

$$\lim_{r\to\infty} \max_{\|\boldsymbol{x}\|=r} \|\boldsymbol{x}\| \left|\langle \nabla u(\boldsymbol{x}), \tfrac{\boldsymbol{x}}{\|\boldsymbol{x}\|}\rangle - \mathrm{i}k_0 u(\boldsymbol{x})\right| = 0. \tag{2.3b}$$

In the following, we assume that the Born approximation of the scattered wave is valid, which holds true for small objects which mildly scatter, cf. [9, 16].

The advantage of the Born approximation is that the solution u of the Helmholtz equation (2.3a) fulfilling the radiation condition (2.3b) can be explicitly written in the form

$$u(\boldsymbol{x}) = \int_{\mathbb{R}^3} \frac{\mathrm{e}^{\mathrm{i}k_0\|\boldsymbol{x}-\boldsymbol{y}\|}}{4\pi\,\|\boldsymbol{x}-\boldsymbol{y}\|} f(\boldsymbol{y}) u^{\mathrm{inc}}(\boldsymbol{y})\,\mathrm{d}\boldsymbol{y},$$

see, for example, [5, Theorem 8.1 and 8.2].

To calculate from the detected field $u(x_1, x_2, r_{\mathrm{M}})$, $(x_1, x_2) \in \mathbb{R}^2$, the scattering potential f, we use the Fourier diffraction theorem, which relates the two-dimensional Fourier transform of the measurement $(x_1, x_2) \mapsto u(x_1, x_2, r_{\mathrm{M}})$ to the three-dimensional Fourier transform of the scattering potential f, see for instance [16, Section 6.3], [28, Theorem 3.1] or [38]. We use here the version [21, Theorem 3.1] derived for the more general case $f \in L^p(\mathbb{R}^3 \to \mathbb{C})$, $p > 1$, which states that

$$\mathcal{F}_{1,2}[u](\boldsymbol{k}, r_{\mathrm{M}}) = \sqrt{\frac{\pi}{2}}\,\frac{\mathrm{i}\mathrm{e}^{\mathrm{i}\kappa(\boldsymbol{k})r_{\mathrm{M}}}}{\kappa(\boldsymbol{k})}\mathcal{F}[f]\left(\boldsymbol{h}(\boldsymbol{k})\right) \quad \text{for all} \quad \boldsymbol{k} = (k_1, k_2) \in \mathcal{B}^2_{k_0}, \tag{2.4}$$

where $\boldsymbol{h}\colon \mathcal{B}^2_{k_0} \to \mathbb{R}^3$ is defined by

$$\boldsymbol{h}(\boldsymbol{k}) \coloneqq \begin{pmatrix} \boldsymbol{k} \\ \kappa(\boldsymbol{k}) - k_0 \end{pmatrix}, \quad \kappa(\boldsymbol{k}) \coloneqq \sqrt{k_0^2 - \|\boldsymbol{k}\|^2}. \tag{2.5}$$

Here the d-dimensional *Fourier transform* is defined for $g\colon \mathbb{R}^3 \to \mathbb{C}$ by

$$\mathcal{F}[g](\boldsymbol{y}) \coloneqq (2\pi)^{-d/2} \int_{\mathbb{R}^d} g(\boldsymbol{x})\,\mathrm{e}^{-\mathrm{i}\langle \boldsymbol{x}, \boldsymbol{y}\rangle}\,\mathrm{d}\boldsymbol{x}, \quad \boldsymbol{y} \in \mathbb{R}^d. \tag{2.6}$$

Moreover, we define the *partial Fourier transform* in the first two components as

$$\mathcal{F}_{1,2}[g](k_1, k_2, x_3) \coloneqq (2\pi)^{-1} \int_{\mathbb{R}^2} g(x_1, x_2, x_3)\,\mathrm{e}^{-\mathrm{i}(x_1k_1 + x_2k_2)}\,\mathrm{d}(x_1, x_2), \quad (k_1, k_2, x_3)^\top \in \mathbb{R}^3.$$

We skip the dependence of the Fourier transform on the dimension in the notation, since this becomes clear from the context. Geometrically, the Fourier diffraction theorem can be interpreted as follows: The left-hand side of (2.4) is the Fourier transform of the (two-dimensional) measured images, while the right-hand side evaluates the three-dimensional Fourier transform of f on a hemisphere whose north pole is the origin $\mathbf{0}$, see the blue hemisphere in Figure 3.

2.2 Motion of the object

In our setting, we record diffraction images while exposing the object of interest to an unknown rigid motion $\Psi\colon [0, T] \times \mathbb{R}^3 \to \mathbb{R}^3$,

$$\Psi_t(\boldsymbol{x}) \coloneqq R_t^\top \boldsymbol{x} + \boldsymbol{d}_t, \tag{2.7}$$

which rotates the object by the rotation matrix $R_t^\top \in \mathrm{SO}(3) \coloneqq \{Q \in \mathbb{R}^{3\times 3} : Q^\top Q = I, \det Q = 1\}$, and translates it by the vector $\boldsymbol{d}_t \in \mathbb{R}^3$. Hereby, we consider the object at time $t = 0$ as the reference object and set correspondingly Ψ_0 to be the identity map, that is, $R_0 \coloneqq I$ and $\boldsymbol{d}_0 \coloneqq \mathbf{0}$. The scattering potential of the object that is exposed to this rigid motion Ψ is then described by the function $t \mapsto f \circ \Psi_t^{-1}$, where the inverse function Ψ_t^{-1} is explicitly given by

$$\Psi_t^{-1}(\boldsymbol{y}) = R_t(\boldsymbol{y} - \boldsymbol{d}_t).$$

The diffraction images are now obtained by continuously illuminating the moving object with the incident wave u^{inc} given by (2.1), and recording the resulting scattered wave (which we will approximate by its Born approximation) on the detector surface $\{\boldsymbol{x} \in \mathbb{R}^3 : x_3 = r_{\mathrm{M}}\}$. We denote by u_t, $t \in [0,T]$, the Born approximation of the wave scattered in the presence of the transformed scattering potential $f \circ \Psi_t^{-1}$, which satisfies the system (2.3) with f replaced by $f \circ \Psi_t^{-1}$, that is, the differential equation

$$\Delta u_t + k_0^2 u_t = -(f \circ \Psi_t^{-1}) u^{\mathrm{inc}}$$

together with the radiation condition

$$\lim_{r\to\infty} \max_{\|\boldsymbol{x}\|=r} \|\boldsymbol{x}\| \left| \left\langle \nabla u_t(\boldsymbol{x}), \tfrac{x}{\|x\|} \right\rangle - \mathrm{i}k_0 u_t(\boldsymbol{x}) \right| = 0.$$

Then the recorded measurement data is given by the function $m\colon [0,T] \times \mathbb{R}^2 \to \mathbb{R}$ with

$$m_t(x_1, x_2) \coloneqq u_t(x_1, x_2, r_{\mathrm{M}}). \tag{2.8}$$

Switching to the Fourier domain with respect to x_1 and x_2, we find by (2.4) for $\boldsymbol{k} \in \mathcal{B}_{k_0}^2$ that

$$\begin{aligned}
\mathcal{F}[m_t](\boldsymbol{k}) &= \sqrt{\frac{\pi}{2}} \frac{\mathrm{i}\mathrm{e}^{\mathrm{i}\kappa(\boldsymbol{k})r_{\mathrm{M}}}}{\kappa(\boldsymbol{k})} \mathcal{F}[f \circ \Psi_t^{-1}]\,(\boldsymbol{h}(\boldsymbol{k})) \\
&= \sqrt{\frac{\pi}{2}} \frac{\mathrm{i}\mathrm{e}^{\mathrm{i}\kappa(\boldsymbol{k})r_{\mathrm{M}}}}{\kappa(\boldsymbol{k})} (2\pi)^{-\frac{3}{2}} \int_{\mathbb{R}^3} f(R_t(\boldsymbol{y} - \boldsymbol{d}_t)) \mathrm{e}^{-\mathrm{i}\langle \boldsymbol{y}, \boldsymbol{h}(\boldsymbol{k})\rangle} \,\mathrm{d}\boldsymbol{y} \\
&= \sqrt{\frac{\pi}{2}} \frac{\mathrm{i}\mathrm{e}^{\mathrm{i}\kappa(\boldsymbol{k})r_{\mathrm{M}}}}{\kappa(\boldsymbol{k})} (2\pi)^{-\frac{3}{2}} \int_{\mathbb{R}^3} f(\tilde{\boldsymbol{y}})\, \mathrm{e}^{-\mathrm{i}\langle R^\top \tilde{\boldsymbol{y}} + \boldsymbol{d}_t, \boldsymbol{h}(\boldsymbol{k})\rangle} \,\mathrm{d}\tilde{\boldsymbol{y}},
\end{aligned}$$

and hence the explicit relation

$$\mathcal{F}[m_t](\boldsymbol{k}) = \sqrt{\frac{\pi}{2}} \frac{\mathrm{i}\mathrm{e}^{\mathrm{i}\kappa(\boldsymbol{k})r_{\mathrm{M}}}}{\kappa(\boldsymbol{k})} \mathcal{F}[f]\,(R_t \boldsymbol{h}(\boldsymbol{k}))\, \mathrm{e}^{-\mathrm{i}\langle \boldsymbol{d}_t, \boldsymbol{h}(\boldsymbol{k})\rangle} \tag{2.9}$$

between the measured data m_t and the unknown scattering potential f.

However, this depends on the unknown parameters R_t and $\boldsymbol{d}_t$ describing the motion of the object. The aim of this paper is to recover both unknown motion parameters. We will first reconstruct the rotation matrix R_t from the absolute values $|\mathcal{F}[m_t]|$ by two different approaches, namely i) the method of common circles, which is in the spirit of the common lines method in ray transforms, and ii) the infinitesimal method for finding changes in the angular velocity during the motion which assumes smooth rotations R_t in time. Relying just on absolute values $|\mathcal{F}[m_t]|$ removes the dependency on the translations $\boldsymbol{d}_t$, which only enter into the Fourier transform as a phase factor. Therefore, we will use the full data $\mathcal{F}[m_t]$ to reconstruct the translation vectors $\boldsymbol{d}_t$ in the second step. Knowing R_t and $\boldsymbol{d}_t$, relation (2.9) can be used to reconstruct the scattering potential f as described in [21].

At this point, we want to stress that the possible reduction of the data to the absolute values $|\mathcal{F}[m_t]|$ for the reconstruction of the rotations is not directly connected to the phaseless optical diffraction measurements, where only the absolute values $|u^{\mathrm{sca}}(x_1, x_2, r_{\mathrm{M}})|$, $x_1, x_2 \in \mathbb{R}$, of the scattered wave u^{sca} are detected, see (2.9).

3 Common Circle Method

Given measurements m_t, $t \in [0,T]$ from (2.8), we can compute their *scaled squared energy* $\nu_t\colon \mathcal{B}_{k_0}^2 \to [0,\infty)$ by

$$\nu_t(\boldsymbol{k}) \coloneqq \frac{2}{\pi} \kappa^2(\boldsymbol{k})\, |\mathcal{F}[m_t](\boldsymbol{k})|^2 \tag{3.1}$$

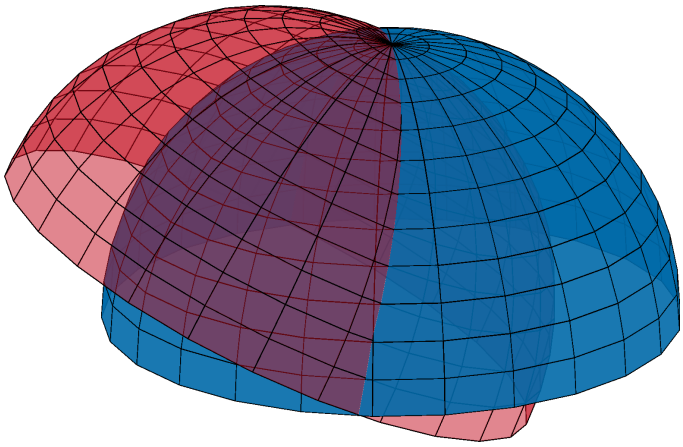

Figure 3: Illustration of the common circles. Two hemispheres $\mathcal{H}_0$ and $\mathcal{H}_t$ intersect in a common circle arc. The north pole of the hemispheres is at $\mathbf{0}$.

with κ from (2.5). According to (2.9), this can be expressed in terms of the scattering potential f as

$$\nu_t(\boldsymbol{k}) = |\mathcal{F}[f](R_t\boldsymbol{h}(\boldsymbol{k}))|^2, \qquad \boldsymbol{k} \in \mathcal{B}^2_{k_0}. \tag{3.2}$$

Thus we observe for $s \neq t$ that

$$\nu_s(\boldsymbol{k}_{s,t}) = \nu_t(\boldsymbol{k}_{t,s}) \tag{3.3}$$

holds for all pairs $(\boldsymbol{k}_{s,t}, \boldsymbol{k}_{t,s}) \in \mathcal{B}^2_{k_0} \times \mathcal{B}^2_{k_0}$ fulfilling

$$R_s\boldsymbol{h}(\boldsymbol{k}_{s,t}) = R_t\boldsymbol{h}(\boldsymbol{k}_{t,s}). \tag{3.4}$$

The aim of this section is to parameterize the curve consisting of all points $\boldsymbol{\sigma}_{s,t} = R_s(\boldsymbol{h}(\boldsymbol{k}_{s,t})) = R_t(\boldsymbol{h}(\boldsymbol{k}_{t,s}))$ and use this afterwards for describing the associated curves $\boldsymbol{k}_{s,t}$ in their respective planes. We will see that the first one is a circular arc in the intersection of two hemispheres, while the second one is an elliptic arc. Having a parameterization with respect to the planes, where the curves are supported, we can switch to their description via the Euler angles of the rotation $R_s^\top R_t$. In Section 6, we will use this description to determine the Euler angles by minimizing a functional based on the matching condition $\nu_s(\boldsymbol{k}_{s,t}) = \nu_t(\boldsymbol{k}_{t,s})$.

We start by defining the sets

$$\mathcal{H}_t := \left\{ R_t\boldsymbol{h}(\boldsymbol{k}) : \boldsymbol{k} \in \mathcal{B}^2_{k_0} \right\}, \quad t \in [0,T],$$

which are by (2.5) the hemispheres with radius k_0 and center $-k_0R_t\boldsymbol{e}^3$, i.e.,

$$\begin{aligned} \mathcal{H}_t &= \{R_t\boldsymbol{y} : \boldsymbol{y} \in \partial\mathcal{B}^3_{k_0}(-k_0\boldsymbol{e}^3),\, y_3 > -k_0\} \\ &= \{\boldsymbol{x} \in \partial\mathcal{B}^3_{k_0}(-k_0R_t\boldsymbol{e}^3) : \langle \boldsymbol{x}, R_t\boldsymbol{e}^3\rangle > -k_0\}, \end{aligned} \tag{3.5}$$

see Figure 3. The intersection $\mathcal{H}_s \cap \mathcal{H}_t$, $s \neq t$ is an arc of a circle and the reason why we call this approach „method of common circles". The following lemma gives its parameterization.

Lemma 3.1 (Parameterization of the common circular arcs) *Let $s,t \in [0,T]$ such that $R_s\boldsymbol{e}^3 \neq \pm R_t\boldsymbol{e}^3$. Then it holds $\mathcal{H}_s \cap \mathcal{H}_t = \{\boldsymbol{\sigma}_{s,t}(\beta) : \beta \in J_{s,t}\}$ with the curve $\boldsymbol{\sigma}_{s,t}\colon J_{s,t} \to \mathbb{R}^3$ defined by*

$$\boldsymbol{\sigma}_{s,t}(\beta) := a_{s,t}(\cos(\beta) - 1)\boldsymbol{v}^1_{s,t} + a_{s,t}\sin(\beta)\boldsymbol{v}^2_{s,t}, \tag{3.6}$$

where we used the positively oriented, orthonormal basis

$$\boldsymbol{v}^1_{s,t} := \frac{R_s\boldsymbol{e}^3 + R_t\boldsymbol{e}^3}{\|R_s\boldsymbol{e}^3 + R_t\boldsymbol{e}^3\|}, \quad \boldsymbol{v}^2_{s,t} := \frac{R_s\boldsymbol{e}^3 \times R_t\boldsymbol{e}^3}{\|R_s\boldsymbol{e}^3 \times R_t\boldsymbol{e}^3\|}, \quad \boldsymbol{v}^3_{s,t} := \frac{R_s\boldsymbol{e}^3 - R_t\boldsymbol{e}^3}{\|R_s\boldsymbol{e}^3 - R_t\boldsymbol{e}^3\|},$$

the radius

$$a_{s,t} \coloneqq \frac{k_0}{2} \left\| R_s \boldsymbol{e}^3 + R_t \boldsymbol{e}^3 \right\|,$$

and the interval

$$J_{s,t} \coloneqq \begin{cases} (-\pi, \pi] & \text{if } \langle R_s \boldsymbol{e}^3, R_t \boldsymbol{e}^3 \rangle \leq 0, \\ (-\beta_{s,t}, \beta_{s,t}) & \text{if } \langle R_s \boldsymbol{e}^3, R_t \boldsymbol{e}^3 \rangle > 0 \end{cases} \quad \text{with} \quad \beta_{s,t} \coloneqq \arccos\left(\frac{\langle R_s \boldsymbol{e}^3, R_t \boldsymbol{e}^3 \rangle - 1}{\langle R_s \boldsymbol{e}^3, R_t \boldsymbol{e}^3 \rangle + 1} \right). \tag{3.7}$$

In particular, we have $\boldsymbol{\sigma}_{s,t}(\beta) = \boldsymbol{\sigma}_{t,s}(-\beta)$ *for all* $\beta \in J_{s,t}$.

Next, according to (3.4), we intend to find the parameterization of $\boldsymbol{\gamma}_{s,t}$ such that $\boldsymbol{\sigma}_{s,t}(\beta) = R_s \boldsymbol{h}(\boldsymbol{\gamma}_{s,t}(\beta))$, $\beta \in J_{s,t}$. Indeed, we see in the following lemma that $\boldsymbol{\gamma}_{s,t}$ is an elliptic arc. The relation between both parameterizations is illustrated in Figure 4, where $P(x_1, x_2, x_3)^\top \coloneqq (x_1, x_2)^\top$. Note that the first case in (3.7) corresponds with when the "lense" in the middle of Figure 4 is fully closed.

Lemma 3.2 (Parameterization by elliptic arcs) *Let* $s, t \in [0, T]$ *such that* $R_s \boldsymbol{e}^3 \neq \pm R_t \boldsymbol{e}^3$ *and let* $\boldsymbol{\sigma}_{s,t}$ *be defined as in* (3.6). *Then, we have*

$$\boldsymbol{\sigma}_{s,t}(\beta) = R_s \boldsymbol{h}(\boldsymbol{\gamma}_{s,t}(\beta)) \quad \text{for all} \quad \beta \in J_{s,t} \tag{3.8}$$

with the elliptic arc $\boldsymbol{\gamma}_{s,t} \colon J_{s,t} \to \mathcal{B}^2_{k_0}$ *determined by*

$$\boldsymbol{\gamma}_{s,t}(\beta) \coloneqq \tilde{a}_{s,t}(\cos(\beta) - 1)\boldsymbol{w}^1_{s,t} + a_{s,t} \sin(\beta) \boldsymbol{w}^2_{s,t}, \tag{3.9}$$

where the directions of the axes are given by

$$\boldsymbol{w}^1_{s,t} \coloneqq \frac{P(R_s^\top R_t \boldsymbol{e}^3)}{\| P(R_s^\top R_t \boldsymbol{e}^3) \|} \quad \text{and} \quad \boldsymbol{w}^2_{s,t} \coloneqq \frac{P(\boldsymbol{e}^3 \times R_s^\top R_t \boldsymbol{e}^3)}{\| P(\boldsymbol{e}^3 \times R_s^\top R_t \boldsymbol{e}^3) \|},$$

and $\tilde{a}_{s,t} \coloneqq \frac{k_0}{2} \| P(R_s^\top R_t \boldsymbol{e}^3) \|$. *In particular, it holds*

$$R_s \boldsymbol{h}(\boldsymbol{\gamma}_{s,t}(\beta)) = R_t \boldsymbol{h}(\boldsymbol{\gamma}_{t,s}(-\beta)) \quad \text{for all } \beta \in J_{s,t}. \tag{3.10}$$

Finally, we want to express $\boldsymbol{\gamma}_{s,t}$ in terms of the Euler angles of rotation matrix $R_s^\top R_t = (R_t^\top R_s)^\top$. Recall that every rotation matrix in $\mathrm{SO}(3)$ can be written (in the z-y-z convention) in the form

$$Q^{(3)}(\varphi)\, Q^{(2)}(\theta)\, Q^{(3)}(\psi)$$

with the Euler angles $\varphi, \psi \in \mathbb{R}/(2\pi\mathbb{Z})$ and $\theta \in [0, \pi]$, where $Q^{(2)}$ and $Q^{(3)}$ denote the rotation matrices

$$Q^{(2)}(\alpha) \coloneqq \begin{pmatrix} \cos(\alpha) & 0 & \sin(\alpha) \\ 0 & 1 & 0 \\ -\sin(\alpha) & 0 & \cos(\alpha) \end{pmatrix} \quad \text{and} \quad Q^{(3)}(\alpha) \coloneqq \begin{pmatrix} \cos(\alpha) & -\sin(\alpha) & 0 \\ \sin(\alpha) & \cos(\alpha) & 0 \\ 0 & 0 & 1 \end{pmatrix},$$

around the $\boldsymbol{e}^2$ and $\boldsymbol{e}^3$ axis, respectively. The Euler angles are uniquely defined if we set $\psi = 0$ for $\theta \in \{0, \pi\}$.

Proposition 3.3 (Representation of $\boldsymbol{\gamma}_{s,t}$ via the Euler angles of $\boldsymbol{R_s^\top R_t}$) *Let* $s, t \in [0, T]$ *such that* $R_s \boldsymbol{e}^3 \neq \pm R_t \boldsymbol{e}^3$ *and let* $(\varphi, \theta, \psi) \in (\mathbb{R}/(2\pi\mathbb{Z})) \times [0, \pi] \times (\mathbb{R}/(2\pi\mathbb{Z}))$ *be the Euler angles of the rotation* $R_s^\top R_t$, *i.e,*

$$R_s^\top R_t = Q^{(3)}(\varphi)\, Q^{(2)}(\theta)\, Q^{(3)}(\psi). \tag{3.11}$$

Then the elliptic arc $\boldsymbol{\gamma}_{s,t}$ *from* (3.9) *is given in terms of the Euler angles by* $\boldsymbol{\gamma}_{s,t}(\beta) = \boldsymbol{\gamma}^{\varphi,\theta}(\beta)$, *where*

$$\boldsymbol{\gamma}^{\varphi,\theta}(\beta) \coloneqq \frac{k_0}{2} \sin(\theta)(\cos(\beta) - 1) \begin{pmatrix} \cos(\varphi) \\ \sin(\varphi) \end{pmatrix} + k_0 \cos(\tfrac{\theta}{2}) \sin(\beta) \begin{pmatrix} -\sin(\varphi) \\ \cos(\varphi) \end{pmatrix}, \quad \beta \in J_{s,t}. \tag{3.12}$$

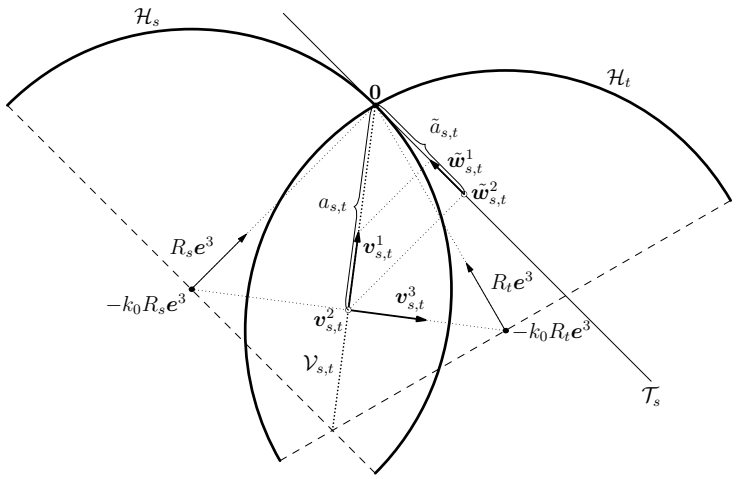

Figure 4: Intersection of two hemispheres $\mathcal{H}_s$ and $\mathcal{H}_t$ in the plane through the centers of the hemispheres and the origin. The circular arc $\mathcal{H}_s \cap \mathcal{H}_t$ lies in the plane $\mathcal{V}_{s,t} = \{\boldsymbol{x} \in \mathbb{R}^3 : \langle \boldsymbol{x}, (R_s - R_t)\boldsymbol{e}^3 \rangle = 0\}$ perpendicular to the line between the centers. It is spanned by $\boldsymbol{v}^j_{s,t}$, $j = 1, 2$ in Lemma 3.1. The basis $\boldsymbol{w}^j_{s,t}$, $j = 1, 2$ of $\mathbb{R}^2$ in Lemma 3.2 is illustrated by the orthogonal projection $\tilde{\boldsymbol{w}}^j_{s,t}$ of $\boldsymbol{v}^j_{s,t}$ to the tangent plane $\mathcal{T}_s$ of $\mathcal{H}_s$ at $\mathbf{0}$. They are explicitly related by $\boldsymbol{w}^j_{s,t} = P(R_s^\top \tilde{\boldsymbol{w}}^j_{s,t})$.

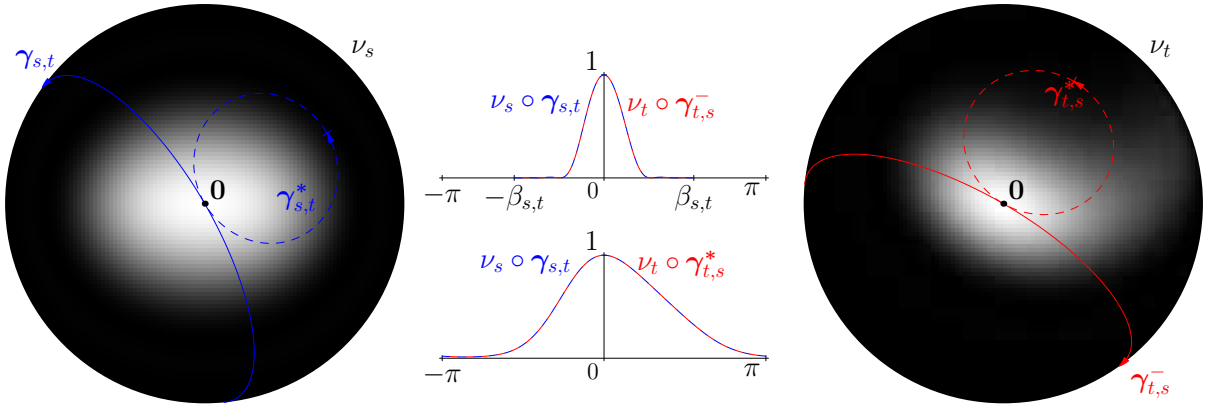

Figure 5: Scaled squared energies ν_s (left) and ν_t (right), see (3.1), for a characteristic function f of an ellipsoid in $\mathbb{R}^3$. For the relative rotation $R_s^\top R_t = Q^{(3)}(\frac{\pi}{6})Q^{(2)}(\frac{\pi}{4})Q^{(3)}(\frac{2\pi}{3})$, we show the paths of the corresponding two elliptic arcs $\boldsymbol{\gamma}_{s,t}$ and $\boldsymbol{\gamma}_{t,s}$ (solid lines), where $\boldsymbol{\gamma}^-_{t,s}$ denotes the reversed elliptic arc $\boldsymbol{\gamma}^-_{t,s}(\beta) := \boldsymbol{\gamma}_{t,s}(-\beta)$, and their dual arcs $\boldsymbol{\gamma}^*_{s,t}$ and $\boldsymbol{\gamma}^*_{t,s}$ (dashed), cf. Proposition 3.4. The relations (3.10) and (3.18) are verified in the center: The top plot shows that the graphs of the scaled squared energy $\nu_s \circ \boldsymbol{\gamma}_{s,t}(\beta)$ along the elliptic arcs in blue and $\nu_t \circ \boldsymbol{\gamma}^-_{t,s}(\beta)$ in red coincide for all β. The same can be seen in the bottom for the dual arcs.

Since the scattering potential f is real-valued, its Fourier transform fulfills the symmetry property

$$\mathcal{F}[f](-\boldsymbol{y}) = \overline{\mathcal{F}[f](\boldsymbol{y})} \quad \text{for all} \quad \boldsymbol{y} \in \mathbb{R}^3, \tag{3.13}$$

which is also known as Friedel's law. Thus we see analogously to (3.3) that $\nu_s(\boldsymbol{k}^*_{s,t}) = \nu_t(\boldsymbol{k}^*_{t,s})$ for all pairs $(\boldsymbol{k}^*_{s,t}, \boldsymbol{k}^*_{t,s}) \in \mathcal{B}^2_{k_0} \times \mathcal{B}^2_{k_0}$ satisfying the *"dual" condition* to (3.4), i.e.,

$$R_s\boldsymbol{h}(\boldsymbol{k}^*_{s,t}) = -R_t\boldsymbol{h}(\boldsymbol{k}^*_{t,s})$$

The parameterization can be handled in a similar way. To this end, we define the reflected hemisphere $-\mathcal{H}_t = \{-\boldsymbol{x} : \boldsymbol{x} \in \mathcal{H}_t\}$ and summarize the results in the following proposition. A graphical illustration is given in Figure 5.

Proposition 3.4 (Parameterization in dual case) *Let $s,t \in [0,T]$ such that $R_s e^3 \neq R_t e^3$. (i) It holds $\mathcal{H}_s \cap (-\mathcal{H}_t) = \{\boldsymbol{\sigma}^*_{s,t}(\beta) : \beta \in J^*_{s,t}\}$ with the curve $\boldsymbol{\sigma}^*_{s,t} \colon J^*_{s,t} \to \mathbb{R}^3$ defined by*

$$\boldsymbol{\sigma}^*_{s,t}(\beta) \coloneqq a^*_{s,t}(\cos(\beta)-1)\boldsymbol{v}^3_{s,t} - a^*_{s,t}\sin(\beta)\boldsymbol{v}^2_{s,t}, \tag{3.14}$$

where

$$a^*_{s,t} \coloneqq \frac{k_0}{2}\left\|R_s e^3 - R_t e^3\right\|$$

and with the interval

$$J^*_{s,t} \coloneqq \begin{cases} (-\pi,\pi] & \text{if } \langle R_s e^3, R_t e^3\rangle \geq 0, \\ (-\beta^*_{s,t},\beta^*_{s,t}) & \text{if } \langle R_s e^3, R_t e^3\rangle < 0 \end{cases} \quad \text{with} \quad \beta^*_{s,t} \coloneqq \arccos\left(\frac{\langle R_s e^3, R_t e^3\rangle + 1}{\langle R_s e^3, R_t e^3\rangle - 1}\right). \tag{3.15}$$

(ii) Further, we have

$$\boldsymbol{\sigma}^*_{s,t}(\beta) = R_s \boldsymbol{h}(\boldsymbol{\gamma}^*_{s,t}(\beta)) \quad \text{for all} \quad \beta \in J^*_{s,t}$$

with the elliptic arc $\boldsymbol{\gamma}^*_{s,t} \colon J^*_{s,t} \to \mathcal{B}^2_{k_0}$ determined by

$$\boldsymbol{\gamma}^*_{s,t}(\beta) \coloneqq -\tilde{a}_{s,t}(\cos(\beta)-1)\boldsymbol{w}^1_{s,t} - a^*_{s,t}\sin(\beta)\boldsymbol{w}^2_{s,t}. \tag{3.16}$$

(iii) Let $(\varphi,\theta,\psi) \in (\mathbb{R}/(2\pi\mathbb{Z})) \times [0,\pi] \times (\mathbb{R}/(2\pi\mathbb{Z}))$ denote the Euler angles of the rotation $R_s^\top R_t$, see (3.11). Then the elliptic arc $\boldsymbol{\gamma}^*_{s,t}$ has the form $\boldsymbol{\gamma}^*_{s,t}(\beta) = \boldsymbol{\gamma}^{*,\varphi,\theta}(\beta)$, where

$$\boldsymbol{\gamma}^{*,\varphi,\theta}(\beta) \coloneqq -\frac{k_0}{2}\sin(\theta)(\cos(\beta)-1)\begin{pmatrix}\cos(\varphi)\\ \sin(\varphi)\end{pmatrix} - k_0\sin(\tfrac{\theta}{2})\sin(\beta)\begin{pmatrix}-\sin(\varphi)\\ \cos(\varphi)\end{pmatrix}. \tag{3.17}$$

In particular, it holds

$$R_s \boldsymbol{h}(\boldsymbol{\gamma}^*_{s,t}(\beta)) = -R_t \boldsymbol{h}(\boldsymbol{\gamma}^*_{t,s}(\beta)) \quad \text{for all } \beta \in J^*_{s,t}. \tag{3.18}$$

So far, we have excluded the cases $R_s e^3 = \pm R_t e^3$. The case $R_s e^3 = \pm R_t e^3$ corresponds with a rotation in x_1 x_2 plane, while the other contains an additional rotation of 180 °. The following proposition shows that these constellations can easily be detected. To this end, we define the matrices

$$\mathrm{S} \coloneqq \begin{pmatrix}1 & 0\\ 0 & -1\end{pmatrix} \qquad \text{and} \qquad \mathrm{Q}(\alpha) \coloneqq \begin{pmatrix}\cos(\alpha) & -\sin(\alpha)\\ \sin(\alpha) & \cos(\alpha)\end{pmatrix}, \quad \alpha \in \mathbb{R}. \tag{3.19}$$

Proposition 3.5 (Special cases $R_s e^3 = \pm R_t e^3$) *(i) Let $s,t \in [0,T]$ such that $R_s e^3 = R_t e^3$. Then we have $R_s^\top R_t = Q^{(3)}(\alpha)$ for some $\alpha \in \mathbb{R}/(2\pi\mathbb{Z})$ and*

$$\nu_s(\mathrm{Q}(\alpha)\boldsymbol{k}) = \nu_t(\boldsymbol{k}) \quad \text{for all} \quad \boldsymbol{k} \in \mathcal{B}^2_{k_0}. \tag{3.20}$$

(ii) Let $s,t \in [0,T]$ such that $R_s e^3 = -R_t e^3$. Then we have $R_s^\top R_t = Q^{(2)}(\pi)Q^{(3)}(\alpha)$ for some $\alpha \in \mathbb{R}/(2\pi\mathbb{Z})$ and

$$\nu_s(\mathrm{SQ}(\alpha)\boldsymbol{k}) = \nu_t(\boldsymbol{k}) \quad \text{for all} \quad \boldsymbol{k} \in \mathcal{B}^2_{k_0}. \tag{3.21}$$

Finally, we can use our findings to formulate our main theorem which says that under certain conditions the Euler angles of $R_s^\top R_t$ can be determined from the matching condition (3.3).

Theorem 3.6 (Reconstruction of Euler angles) *Let $s,t \in [0,T]$ such that neither (3.20) nor (3.21) hold for any $\alpha \in \mathbb{R}/(2\pi\mathbb{Z})$. Furthermore, assume that there exist unique angles $\varphi,\psi \in \mathbb{R}/(2\pi\mathbb{Z})$ and $\theta \in [0,\pi]$ such that*

$$\nu_s(\boldsymbol{\gamma}^{\varphi,\theta}(\beta)) = \nu_t(\boldsymbol{\gamma}^{\pi-\psi,\theta}(-\beta)) \quad \text{for all} \quad \beta \in [-\tfrac{\pi}{2},\tfrac{\pi}{2}] \quad \text{and} \tag{3.22}$$

$$\nu_s(\boldsymbol{\gamma}^{*,\varphi,\theta}(\beta)) = \nu_t(\boldsymbol{\gamma}^{*,\pi-\psi,\theta}(\beta)) \quad \text{for all} \quad \beta \in [-\tfrac{\pi}{2},\tfrac{\pi}{2}], \tag{3.23}$$

where $\boldsymbol{\gamma}^{\varphi,\theta}$ and $\boldsymbol{\gamma}^{*,\varphi,\theta}$ are defined in (3.12) and (3.17), respectively. Then we have

$$R_s^\top R_t = Q^{(3)}(\varphi)Q^{(2)}(\theta)Q^{(3)}(\psi). \tag{3.24}$$

Since the curves $\boldsymbol{\gamma}^*$ in (3.23) are traversed in the same direction and the curves $\boldsymbol{\gamma}$ in (3.22) in the opposite direction, they can be distinguished. Hence, under the uniqueness assumptions in Theorem 3.6, it suffices if only one of the equations (3.22) or (3.23) is fulfilled in order to obtain the Euler angles of $R_s^\top R_t$. One could also obtain a slightly stronger result by replacing the interval $[-\frac{\pi}{2}, \frac{\pi}{2}]$ in Theorem 3.6 by a larger one depending on θ, cf. (3.7) and (3.15).

Nevertheless, the reconstruction relies on the uniqueness of the elliptic arcs with property (3.22), which might fail if the function f has too much symmetry. For example, if f is rotationally invariant, then so is its Fourier transform $\mathcal{F}[f]$, and therefore $\nu_s = \nu_t$ for all $s, t \in [0, T]$, which clearly makes it impossible to reconstruct any rotation. In the generic case, however, we expect that this problem does not occur and neither does it in our numerical examples. Our variational model in Section 6 exploits both the curves and their dual versions.

We finish this section by two different remarks concerning common lines and common circles.

Remark 3.7 (Methods of common circles and common lines) We can obtain the relative rotation $R_s^\top R_t$, which the object undergoes at only *two* different time steps t and s, from two data sets ν_s and ν_t. This is in contrast to the common line method for the ray transform [8], which requires to detect the intersection of pairwise common lines in images from at least *three* different rotations in order to calculate the relative rotations, see Figure 1. This is also apparent from the fact that our common circle formulation contains the three Euler angles from the three dimensional manifold SO(3) as parameters, whereas in the common line method for the ray transform there are only the two parameters parameterizing the lines through the origin.

Remark 3.8 (Stereographic projection) Instead of detecting elliptic arcs in the images ν_t, we may use a different parameterization in which the arcs become straight lines. Such a parameterization is provided by the stereographic projection of the hemisphere $\mathcal{H}_t \setminus \{\mathbf{0}\}$ from the origin onto its equatorial plane $\{\boldsymbol{x} \in \mathbb{R}^3 : \langle \boldsymbol{x}, R_t \boldsymbol{e}^3 \rangle = -k_0\}$. The stereographic projection maps the common circle (3.6) to a straight line in the equatorial plane. Then we can detect the rotations $R_s^\top R_t$ by finding common lines in the transformed, two-dimensional data. The details are provided in Appendix D.

4 Infinitesimal Common Circle Method

In this section, we make the additional assumption that the rotations R_t to which the object is exposed via the transformation (2.7) depend smoothly on the time $t \in [0, T]$, i.e., we assume that $R \in C^1([0, T] \to \mathrm{SO}(3))$, where we consider SO(3) as submanifold of $\mathbb{R}^{3\times 3}$. Since the fact that the scattering potential f has compact support implies by the Paley–Wiener theorem that $\mathcal{F}[f] \in C^\infty(\mathbb{R}^3 \to \mathbb{C})$, we thus have that $\nu_t(\boldsymbol{k})$ is continuously differentiable both in time t and space $\boldsymbol{k}$.

In this setting, we can describe the relative rotation $R_s^\top R_t$ between two time steps $s, t \in [0, T]$ in the limit $s \to t$ by the derivative $(R_t')^\top R_t = (R_t^\top R_t')^\top$, where R_t' denotes the time derivative of R_t at $t \in [0, T]$. The derivative of the defining identity $R_t^\top R_t = I$ with respect to t is given by $R_t^\top R_t' + (R_t^\top R_t')^\top = 0$. Hence the *angular velocity matrix* $W_t \coloneqq R_t^\top R_t'$ is skew-symmetric and thus can be described by three parameters. The *angular velocity* $\boldsymbol{\omega}_t \colon [0, T] \to \mathbb{R}^3$ of the rotational motion R_t, cf. [25, Chapter VI], is defined by

$$R_t^\top R_t' \boldsymbol{y} = \boldsymbol{\omega}_t \times \boldsymbol{y} \quad \text{for all } t \in [0, T],\ \boldsymbol{y} \in \mathbb{R}^3. \tag{4.1}$$

In particular, we have

$$W_t = \begin{pmatrix} 0 & -\omega_{t,3} & \omega_{t,2} \\ \omega_{t,3} & 0 & -\omega_{t,1} \\ -\omega_{t,2} & \omega_{t,1} & 0 \end{pmatrix}, \quad \text{where} \quad \boldsymbol{\omega}_t \coloneqq (\omega_{t,1}, \omega_{t,2}, \omega_{t,3})^\top. \tag{4.2}$$

In the following, we want to reconstruct the angular velocity $\boldsymbol{\omega}_t$ of the rigid motion at a time $t \in [0,T]$ from the behavior of the data ν in the vicinity of the time t, more precisely from the first derivatives of ν at the time t. We will utilize a similar approach as done for the ray transform in [8].

For the reconstruction, it is convenient to express $\boldsymbol{\omega}_t$ in cylindrical coordinates

$$\boldsymbol{\omega}_t = \begin{pmatrix} \rho_t \boldsymbol{\phi}_t \\ \zeta_t \end{pmatrix} = \begin{pmatrix} \rho_t \phi_{t,1} \\ \rho_t \phi_{t,2} \\ \zeta_t \end{pmatrix} \tag{4.3}$$

with the azimuth direction $\boldsymbol{\phi}_t \in \mathbb{S}^1_+ := \{(\cos(\alpha), \sin(\alpha))^\top : \alpha \in [0,\pi)\}$, the cylindrical radius $\rho_t \in \mathbb{R}$, and the third component $\zeta_t \in \mathbb{R}$. Note that, in contrast to conventional cylindrical coordinates, we allow negative radii ρ_t, but restrict in exchange $\boldsymbol{\phi}_t$ to $\mathbb{S}^1_+$.

To obtain the reconstruction formula, we consider for values $s,t \in [0,T]$ with $R_s \boldsymbol{e}^3 \neq \pm R_t \boldsymbol{e}^3$ again the elliptic arcs $\boldsymbol{\gamma}_{s,t}$ in (3.9) fulfilling the identity

$$\nu_s(\boldsymbol{\gamma}_{s,t}(\beta)) = \nu_t(\boldsymbol{\gamma}_{t,s}(-\beta)), \tag{4.4}$$

in (3.10). Taking therein for fixed $t \in [0,T]$ the limit $s \to t$, we find that the relation

$$\lim_{s \to t} \frac{\nu_s(\boldsymbol{\gamma}_{s,t}(\beta)) - \nu_t(\boldsymbol{\gamma}_{t,s}(-\beta))}{s-t} = 0 \tag{4.5}$$

holds, which gives us a relation between the first order derivatives of the function $(t, \boldsymbol{k}) \mapsto \nu_t(\boldsymbol{k})$ involving only the angular velocity $\boldsymbol{\omega}_t$ of the rotations at the time t. As we will see, this first order part of (4.4) contains enough information to recover the angular velocity and therefore the whole rotations. This method can thus be seen as an infinitesimal version of Theorem 3.6. Rewriting the relation (4.5) directly by expanding the functions in Taylor series in the variable s around the point t would be rather tedious, similar to the calculation in [8] for the ray transform. Therefore, we will simply verify the following lemma via direct computation.

Lemma 4.1 (Infinitesimal common circle relation) *Let the rotations $R \in C^1([0,T] \to \mathrm{SO}(3))$ be continuously differentiable and the associated angular velocities $\boldsymbol{\omega}_t \in \mathbb{R}^3$ be written in cylindrical coordinates (4.3). Then we have for every $r \in (-k_0, k_0)$ and $t \in [0,T]$ the relation*

$$\partial_t \nu_t(r\boldsymbol{\phi}_t) = \left(\rho_t \left(k_0 - \sqrt{k_0^2 - r^2}\right) + r\zeta_t\right) \left\langle \nabla \nu_t(r\boldsymbol{\phi}_t), \begin{pmatrix} -\phi_{t,2} \\ \phi_{t,1} \end{pmatrix} \right\rangle, \tag{4.6}$$

where $\partial_t \nu_t$ denotes the partial derivative of ν_t with respect to t, and $\nabla \nu_t(\boldsymbol{k})$ the gradient with respect to $\boldsymbol{k}$.

This gives rise to the following reconstruction method. For the reconstruction to be unique, we require that (4.6) has a unique solution $(\rho_t, \boldsymbol{\phi}_t, \zeta_t) \in \mathbb{R} \times \mathbb{S}^1_+ \times \mathbb{R}$, which consists of the components of the angular velocity we want to reconstruct. If the object (and therefore f) is asymmetric, it seems reasonable to assume there is indeed a unique solution $(\rho_t, \boldsymbol{\phi}_t, \zeta_t)$ to (4.6), which happens in all our numerical simulations. Conditions for the unique reconstructability of f are discussed in [20, 22].

Theorem 4.2 (Reconstruction of the angular velocity $\boldsymbol{\omega}_t$) *Let the rotations matrices $R \in C^1([0,T] \to \mathrm{SO}(3))$ be continuously differentiable and $t \in [0,T]$. Let further $\boldsymbol{\phi} \in \mathbb{S}^1_+$ be a unique direction with the property that there exist parameters $\rho, \zeta \in \mathbb{R}$ such that*

$$\partial_t \nu_t(r\boldsymbol{\phi}) = \left(\rho \left(k_0 - \sqrt{k_0^2 - r^2}\right) + r\zeta\right) \left\langle \nabla \nu_t(r\boldsymbol{\phi}), \begin{pmatrix} -\phi_2 \\ \phi_1 \end{pmatrix} \right\rangle \quad \text{for all} \quad r \in (-k_0, k_0).$$

Provided that the set

$$\mathcal{N}_t := \left\{ r \in (-k_0, k_0) \setminus \{0\} : \left\langle \nabla \nu_t(r\boldsymbol{\phi}), \begin{pmatrix} -\phi_2 \\ \phi_1 \end{pmatrix} \right\rangle \neq 0 \right\}$$

contains at least two elements, then the angular velocity (4.3) *is given by* $\boldsymbol{\omega}_t = (\rho\boldsymbol{\phi}, \zeta)^\top$.

Proof: From Lemma 4.1, we find that the uniqueness implies that $\boldsymbol{\phi}_t = \boldsymbol{\phi}$ and therefore also

$$\rho + \frac{r}{k_0 - \sqrt{k_0^2 - r^2}}\,\zeta = \rho_t + \frac{r}{k_0 - \sqrt{k_0^2 - r^2}}\,\zeta_t \quad \text{for all} \quad r \in \mathcal{N}_t.$$

Since the function $(-k_0, k_0) \setminus \{0\} \to \mathbb{R} \setminus [-1, 1]$, $r \mapsto r/(k_0 - \sqrt{k_0^2 - r^2})$ is bijective, we have $\rho = \rho_t$ and $\zeta = \zeta_t$ if the equation is satisfied for two different values r. □

An alternative version of the last theorem via stereographic projection is found in Appendix D.2. Once we have reconstructed the angular velocity $\boldsymbol{\omega}_t$ by the above theorem, we can obtain the rotation matrices R_t as follows.

Theorem 4.3 (Reconstruction of the rotation from the angular velocity) *Let the rotations* $R \in C^1([0, T] \to \mathrm{SO}(3))$ *be continuously differentiable with associated angular velocity* $\boldsymbol{\omega}$, *see* (4.1). *Then* R *is the unique solution of the linear initial value problem*

$$\begin{aligned} R_t' &= R_t W_t, \quad t \in (0, T), \\ R_0 &= I, \end{aligned} \tag{4.7}$$

where the skew-symmetric matrix $W_t \in \mathbb{R}^{3\times 3}$ *is defined in* (4.2).

Proof: The equation (4.7) follows directly from the definition (4.1) of the angular velocity. As a linear ordinary differential equation, the initial value problem (4.7) has a unique solution. □

Remark 4.4 (Differences to infinitesimal common line method) In contrast to the infinitesimal common line method [8] for the ray transform (1.1), which requires third order derivatives of the data function, we only need first order derivatives of ν in order to reconstruct the angular velocity completely. Furthermore, we can uniquely recover the rotation, whereas for the ray transform there are always two possible solutions corresponding to a reflection in the direction of the imaging wave.

5 Reconstruction of the Translations

So far, we have only considered the computation of the rotations R_t, $t \in [0, T]$, in the motion (2.7), which we could obtain from the absolute values of the Fourier transforms of our measurements m_t, $t \in [0, T]$, that is, from the scaled squared energy ν_t defined in (3.1). To recover the translations $\boldsymbol{d}_t \in \mathbb{R}^3$, we need to use in addition the phase information in our measurements m_t, see (2.8). Therefore we define the *scaled measurement data* $\mu_t \colon \mathcal{B}_{k_0}^2 \to \mathbb{C}$ by

$$\mu_t(\boldsymbol{k}) := -\mathrm{i}\sqrt{\frac{2}{\pi}}\,\kappa(\boldsymbol{k}) \mathrm{e}^{-\mathrm{i}\kappa(\boldsymbol{k}) r_{\mathrm{M}}} \mathcal{F}[m_t](\boldsymbol{k}). \tag{5.1}$$

According to (2.9) this can be expressed in terms of the scattering potential f, the rotation $R_t \in \mathrm{SO}(3)$, and the translation $\boldsymbol{d}_t \in \mathbb{R}^3$ by

$$\mu_t(\boldsymbol{k}) = \mathcal{F}[f]\left(R_t \boldsymbol{h}(\boldsymbol{k})\right) \mathrm{e}^{-\mathrm{i}\langle \boldsymbol{d}_t, \boldsymbol{h}(\boldsymbol{k})\rangle}. \tag{5.2}$$

If we have already reconstructed the rotations R_t, then we know by (3.10) and (3.18) the elliptic arcs $\boldsymbol{\gamma}_{s,t}$ and the duals $\boldsymbol{\gamma}_{s,t}^*$ along which the values of the scaled squared energies $\nu_s = |\mu_s|^2$ and $\nu_t = |\mu_t|^2$ coincide. Therefore, the corresponding values of μ_s and μ_t only differ by a phase factor, which depends on the translation vectors $\boldsymbol{d}_s$ and $\boldsymbol{d}_t$. We compute their relation explicitly in the following lemma.

Lemma 5.1 (Complex phase shift along the common circles) *Let $s,t \in [0,T]$ such that $R_s\boldsymbol{e}^3 \neq \pm R_t\boldsymbol{e}^3$ and let $\boldsymbol{\gamma}_{s,t}$ and $\boldsymbol{\gamma}_{t,s}$ be the elliptic arcs defined in Lemma 3.2 and $\boldsymbol{\sigma}_{s,t} = R_s(\boldsymbol{h}\circ\boldsymbol{\gamma}_{s,t})$ be the corresponding common circular arc introduced in Lemma 3.1. Moreover, let $\boldsymbol{\gamma}^*_{s,t}$ and $\boldsymbol{\gamma}^*_{t,s}$ be the dual elliptic arcs and $\boldsymbol{\sigma}^*_{s,t} = R_s(\boldsymbol{h}\circ\boldsymbol{\gamma}^*_{s,t})$ be the corresponding dual common circular arc as defined in Proposition 3.4. Then we have*

(i) for every $\beta \in J_{s,t}$ with $\mu_s(\boldsymbol{\gamma}_{s,t}(\beta)) \neq 0$ that

$$\mathrm{e}^{\mathrm{i}\langle R_t\boldsymbol{d}_t - R_s\boldsymbol{d}_s, \boldsymbol{\sigma}_{s,t}(\beta)\rangle} = \frac{\mu_s(\boldsymbol{\gamma}_{s,t}(\beta))}{\mu_t(\boldsymbol{\gamma}_{t,s}(-\beta))}. \tag{5.3}$$

(ii) for every $\beta \in J^*_{s,t}$ with $\mu_s(\boldsymbol{\gamma}^*_{s,t}(\beta)) \neq 0$ that

$$\mathrm{e}^{\mathrm{i}\left\langle R_t\boldsymbol{d}_t - R_s\boldsymbol{d}_s, \boldsymbol{\sigma}^*_{s,t}(\beta)\right\rangle} = \frac{\mu_s(\boldsymbol{\gamma}^*_{s,t}(\beta))}{\overline{\mu_t(\boldsymbol{\gamma}^*_{t,s}(\beta))}}. \tag{5.4}$$

In the degenerate cases $R_s\boldsymbol{e}^3 = \pm R_t\boldsymbol{e}^3$, a similar relation holds on the whole hemisphere.

Lemma 5.2 (Special cases $\boldsymbol{R_s e^3 = \pm R_t e^3}$) *Let $R_s^\top R_t$ be known for some $s,t \in [0,T]$, and let Q and S be given in (3.19).*

(i) If $R_t\boldsymbol{e}^3 = R_s\boldsymbol{e}^3$, then we have for all $\boldsymbol{k} \in \mathcal{B}^2_{k_0}$ with $\mu_s(\boldsymbol{k}) \neq 0$ that

$$\mathrm{e}^{\mathrm{i}\langle R_t\boldsymbol{d}_t - R_s\boldsymbol{d}_s, R_s\boldsymbol{h}(\boldsymbol{k})\rangle} = \frac{\mu_s(\boldsymbol{k})}{\mu_t(\mathrm{Q}(-\alpha)\boldsymbol{k})} \tag{5.5}$$

with some $\alpha \in \mathbb{R}/(2\pi\mathbb{Z})$ fulfilling $R_s^\top R_t\boldsymbol{e}^3 = Q^{(3)}(\alpha)$ according to Proposition 3.5 (i).

(ii) If $R_t\boldsymbol{e}^3 = -R_s\boldsymbol{e}^3$, then we have for all $\boldsymbol{k} \in \mathcal{B}^2_{k_0}$ with $\mu_s(\boldsymbol{k}) \neq 0$ that

$$\mathrm{e}^{\mathrm{i}\langle R_t\boldsymbol{d}_t - R_s\boldsymbol{d}_s, R_s\boldsymbol{h}(\boldsymbol{k})\rangle} = \frac{\mu_s(\boldsymbol{k})}{\overline{\mu_t(\mathrm{Q}(-\alpha)S\boldsymbol{k})}} \tag{5.6}$$

with some $\alpha \in \mathbb{R}/(2\pi\mathbb{Z})$ fulfilling $R_s^\top R_t\boldsymbol{e}^3 = Q^{(2)}(\pi)Q^{(3)}(\alpha)$ according to Proposition 3.5 (ii).

In contrast to data of the ray transform (1.1), where the measurements are invariant to the object's position in direction of the incident wave, the diffraction data are not invariant with respect to the third component of the translations. By the following theorem, we can uniquely recover the translation vectors $\boldsymbol{d}_t$, $t \in [0,T]$, from the equations (5.3), (5.4), (5.5), and (5.6).

Theorem 5.3 (Reconstruction of the translation) *Let the relative rotation $R_s^\top R_t$ be known for some $s,t \in [0,T]$.*

(i) If $R_s\boldsymbol{e}^3 \neq \pm R_t\boldsymbol{e}^3$, then the relative translation $R_s^\top R_t\boldsymbol{d}_t - \boldsymbol{d}_s$ is uniquely determined from the scaled measurements μ_s and μ_t by the equations (5.3) and (5.4).

(ii) If $R_s\boldsymbol{e}^3 = \pm R_t\boldsymbol{e}^3$, then the relative translation $R_s^\top R_t\boldsymbol{d}_t - \boldsymbol{d}_s$ is uniquely determined from the scaled measurements μ_s and μ_t by the equation (5.5) or (5.6).

Thus, if f is sufficiently asymmetric so that we find for each $t \in [0,T]$ a time $s \in [0,T]$, for which R_s was already reconstructed (starting from the normalization $R_0 = I$), and such that there either

exist unique elliptic arcs in ν_s and ν_t as described in Theorem 3.6, or we have $R_s\boldsymbol{e}^3 = \pm R_t\boldsymbol{e}^3$ and there exists a unique angle α fulfilling either (3.20) or (3.21), then Proposition 3.5 and Theorem 3.6 determine uniquely the rotation R_t. With this knowledge, we get from Theorem 5.3 with $\boldsymbol{d}_0 = \boldsymbol{0}$ all the translations $\boldsymbol{d}_t$, $t \in [0,T]$, and therefore the complete motion Ψ of our object, introduced in (2.7).

The following remark gives an interesting relation to higher order moment methods.

Remark 5.4 (Relation to higher order moment methods) We can also detect the optical center $\mathcal{C} \in \mathbb{R}^3$ of the object, that is, the ratio

$$\mathcal{C} := \frac{\int_{\mathbb{R}^3} \boldsymbol{x} f(\boldsymbol{x}) \,\mathrm{d}x}{\int_{\mathbb{R}^3} f(\boldsymbol{x}) \,\mathrm{d}x} = \frac{\mathrm{i}\nabla\mathcal{F}[f](\boldsymbol{0})}{\mathcal{F}[f](\boldsymbol{0})}$$

of the first and the zeroth moment of the function f, from the transformed data μ_t, see (5.1), by realizing that

$$\frac{\mathrm{i}\partial_{k_i}\mu_t(\boldsymbol{0})}{\mu_t(\boldsymbol{0})} = \frac{\mathrm{i}\left\langle \nabla\mathcal{F}[f](\boldsymbol{0}), R_t\boldsymbol{e}^i\right\rangle}{\mathcal{F}[f](\boldsymbol{0})} + d_{t,i} = \left\langle \mathcal{C}, R_t\boldsymbol{e}^i\right\rangle + d_{t,i}, \quad i \in \{1,2\}.$$

If we have a time $t \in [0,T]$ for which the rotation R_t has a rotation axis different from $\mathbb{R}\boldsymbol{e}^3$, this allows us (other than from data of the ray transform) to fully recover the point $\mathcal{C} \in \mathbb{R}^3$ without the need of first reconstructing f. Theoretically, this approach also provides a reconstruction of arbitrary moments of the function f by incorporating higher-order derivatives of μ_t, which was used in [22] to prove the unique reconstructability of f.

6 Reconstruction Methods

Based on our previous results we can provide concrete reconstruction methods for the motion parameters now. We start by considering the rotations and continue with translations afterwards.

6.1 Reconstruction of the rotation

For reconstructing the rotations R_t, we can utilize the common circle method in Section 3 and its infinitesimal counterpart in Section 4. Here, we assume that ν_t from (3.1) are given.

6.1.1 Direct common circle method

We utilize Theorem 3.6 to find the common circles and therefore reconstruct the rotation R_t. We want to find the Euler angles $(\varphi,\theta,\psi) \in (\mathbb{R}/(2\pi\mathbb{Z})) \times [0,\pi] \times (\mathbb{R}/(2\pi\mathbb{Z}))$ of the rotation $R_s^\top R_t$ by solving (3.22) and (3.23). When working with measured data, it is unlikely that these equations hold exactly, therefore we propose a least-squares approach: we aim to minimize the functional

$$\mathcal{E}_{s,t}(\varphi,\theta,\psi) := \int_{-\pi/2}^{\pi/2} \left|\nu_t(\boldsymbol{\gamma}^{\pi-\psi,\theta}(-\beta)) - \nu_s(\boldsymbol{\gamma}^{\varphi,\theta}(\beta))\right|^2 + \left|\nu_t(\boldsymbol{\gamma}^{*,\pi-\psi,\theta}(\beta)) - \nu_s(\boldsymbol{\gamma}^{*,\varphi,\theta}(\beta))\right|^2 \mathrm{d}\beta \tag{6.1}$$

over $\varphi,\psi \in \mathbb{R}/(2\pi\mathbb{Z})$ and $\theta \in [0,\pi]$, where the elliptic arcs $\boldsymbol{\gamma}^{\varphi,\theta}$ and $\boldsymbol{\gamma}^{*,\varphi,\theta}$ are given in (3.12) and (3.17). If ν_t is given on a grid, it needs to be interpolated in order to evaluate $\nu_t(\boldsymbol{\gamma}^{\pi-\psi,\theta}(-\beta))$ in (6.1). Furthermore, the integral in (6.1) can be discretized via quadrature.

We consider the minimizer of $\mathcal{E}_{s,t}$ as a good approximation of the Euler angles (3.11) of the rotation $R_s^\top R_t$. Using that $R_0 = I$, we compute the minimizer of $\mathcal{E}_{0,t}$ to obtain $R_0^\top R_t = R_t$ for all t by Algorithm 1.

Algorithm 1: Reconstruction of the rotation R_t with the direct common circle method

Input: Scaled squared energy ν_t, discretization parameter $N \in \mathbb{N}$, grid of Euler angles $(\varphi_\ell, \theta_\ell, \psi_\ell) \subset [0, 2\pi) \times [0, \pi] \times [0, 2\pi)$, $\ell = 1, \dots, L$.

Set the grid $\beta_n \coloneqq n\pi/N$, $n = -N, \dots, N$;

for $\ell = 1, \dots, L$ **do**

  Compute $\mathtt{E}(\ell) \coloneqq$
  $\sum_{n=-N}^{N} \left|\nu_t(\boldsymbol{\gamma}^{\pi-\psi_\ell,\theta_\ell}(-\beta_n)) - \nu_0(\boldsymbol{\gamma}^{\varphi_\ell,\theta_\ell}(\beta_n))\right|^2 + \left|\nu_t(\boldsymbol{\gamma}^{*,\pi-\psi_\ell,\theta_\ell}(\beta_n)) - \nu_0(\boldsymbol{\gamma}^{*,\varphi_\ell,\theta_\ell}(\beta_n))\right|^2$
  using an interpolation of ν_t and ν_0;

end

Compute $\hat{\ell} = \arg\min_\ell \mathtt{E}$;

Output: Rotation $R_t \approx Q^{(3)}(\varphi_{\hat{\ell}}) Q^{(2)}(\theta_{\hat{\ell}}) Q^{(3)}(\psi_{\hat{\ell}})$, see (3.11).

The accuracy of R_t may be improved by incorporating reconstructions of $R_s^\top R_t$ for all s, t, similarly to cryo-EM [37]. The minimization of $\mathcal{E}_{s,t}$ is a three-dimensional, non-linear and non-convex optimization problem, for which we can use a brute force method by searching on a grid of SO(3). The computation of the minimum of (6.1) becomes much more efficient if we have good initial values (φ, θ, ψ), which can be obtained by the infinitesimal method in the next subsection.

6.1.2 Infinitesimal common circle method

The reconstruction is done in two steps. First, we reconstruct the angular velocity, second we use this to find the rotation.

Angular velocity Let $t \in (0, T)$ be arbitrary but fixed. We reconstruct the angular velocity $\boldsymbol{\omega}_t = (\rho_t \cos(\phi_t), \rho_t \sin(\phi_t), \zeta_t)^\top$, $\rho_t, \zeta_t \in \mathbb{R}$, $\phi_t \in [0, \pi)$ using Theorem 4.2. In particular, we construct a functional that we minimize over (ρ, ϕ, ζ) in order to find the exact parameters $(\rho_t, \phi_t, \zeta_t)$. For $r \in (-k_0, k_0)$ and $\phi \in [0, \pi)$, we set

$$\begin{aligned} g_\phi(r) &\coloneqq \partial_t \nu_t(r\cos(\phi), r\sin(\phi)), \\ p_\phi(r) &\coloneqq \left(k_0 - \sqrt{k_0^2 - r^2}\right) \left\langle \nabla \nu_t(r\cos(\phi), r\sin(\phi)), \begin{pmatrix} -\sin(\phi) \\ \cos(\phi) \end{pmatrix} \right\rangle, \\ q_\phi(r) &\coloneqq r \left\langle \nabla \nu_t(r\cos(\phi), r\sin(\phi)), \begin{pmatrix} -\sin(\phi) \\ \cos(\phi) \end{pmatrix} \right\rangle. \end{aligned} \tag{6.2}$$

Note that these functions are indeed continuous and they are obtained by differentiating the scaled squared energy ν_t. Then relation (4.6) of the angular velocity can be written as

$$g_{\phi_t}(r) = \rho_t\, p_{\phi_t}(r) + \zeta_t\, q_{\phi_t}(r), \qquad r \in (-k_0, k_0). \tag{6.3}$$

As in the direct method, we use a least squares approach to solve (6.3) in order to recover the quantities ρ_t, ϕ_t and ζ_t. We want to minimize the functional

$$\mathcal{J}(\rho, \phi, \zeta) \coloneqq \|g_\phi - \rho\, p_\phi - \zeta\, q_\phi\|^2_{L^2(-k_0, k_0)}, \qquad \rho, \zeta \in \mathbb{R},\ \phi \in [0, \pi),$$

which vanishes according to (6.3) for $(\rho, \phi, \zeta) = (\rho_t, \phi_t, \zeta_t)$, so that the desired angular velocity $\boldsymbol{\omega}_t$ is indeed a minimizer of $\mathcal{J}_t$.

We minimize $\mathcal{J}$ by a brute-force method. For every $\phi \in [0, \pi)$ on a fixed grid, we compute the minimizer of the functional $\mathcal{J}_\phi \colon \mathbb{R}^2 \to \mathbb{R}$, $\mathcal{J}_\phi(\rho, \zeta) \coloneqq \mathcal{J}(\rho, \phi, \zeta)$, which we can explicitly get from the optimality condition

$$\mathbf{0} = \nabla \mathcal{J}_\phi(\rho, \zeta) = \begin{pmatrix} \frac{\partial}{\partial \rho} \mathcal{J}_\phi(\rho, \zeta) \\ \frac{\partial}{\partial \zeta} \mathcal{J}_\phi(\rho, \zeta) \end{pmatrix} = 2 \begin{pmatrix} \rho \langle p_\phi, p_\phi \rangle - \langle g_\phi, p_\phi \rangle + \zeta \langle p_\phi, q_\phi \rangle \\ \zeta \langle q_\phi, q_\phi \rangle - \langle g_\phi, q_\phi \rangle + \rho \langle p_\phi, q_\phi \rangle \end{pmatrix},$$

where $\langle \cdot, \cdot \rangle$ denotes the inner product on $L^2((-k_0, k_0) \to \mathbb{R})$ here. Provided that the functions p_ϕ and q_ϕ are linearly independent in $L^2((-k_0, k_0) \to \mathbb{R})$, so that by Cauchy-Schwarz' inequality $\|p_\phi\|_{L^2} \|q_\phi\|_{L^2} \neq |\langle p_\phi, q_\phi \rangle|$, the above system has a unique solution. The unique minimizer $(\hat{\rho}(\phi), \hat{\zeta}(\phi))$ is then given by

$$\begin{pmatrix} \hat{\rho}(\phi) \\ \hat{\zeta}(\phi) \end{pmatrix} = \begin{pmatrix} \langle p_\phi, p_\phi \rangle & \langle p_\phi, q_\phi \rangle \\ \langle p_\phi, q_\phi \rangle & \langle q_\phi, q_\phi \rangle \end{pmatrix}^{-1} \begin{pmatrix} \langle g_\phi, p_\phi \rangle \\ \langle g_\phi, q_\phi \rangle \end{pmatrix}. \tag{6.4}$$

For every $\phi \in [0, \pi)$ on the grid, we thus first calculate the value

$$j(\phi) := \min_{\rho, \zeta \in \mathbb{R}} \mathcal{J}(\rho, \phi, \zeta) = \mathcal{J}(\hat{\rho}(\phi), \phi, \hat{\zeta}(\phi)), \tag{6.5}$$

then we take as approximation of the angle ϕ_t in the angular velocity $\boldsymbol{\omega}_t$ the minimizer $\hat{\phi} \in [0, \pi)$ of $j(\phi)$ on this grid, and pick $\hat{\rho}(\hat{\phi})$ and $\hat{\zeta}(\hat{\phi})$ as approximations for ρ_t and ζ_t. The reconstruction is summarized in Algorithm 2.

Algorithm 2: Reconstruction of the angular velocity $\boldsymbol{\omega}_t$ with the infinitesimal method

Input: Scaled squared energy $\nu_t(r_n \cos \phi_\ell, r_n \sin \phi_\ell)$ from (3.1) on a polar grid $r_n \in [0, k_0)$, $n = 1, \dots, N$, and $\phi_\ell \in [0, \pi)$, $\ell = 1, \dots, L$.

for $\ell = 1, \dots, L$ **do**

- Compute the functions $g_{\phi_\ell}(r_n)$, $p_{\phi_\ell}(r_n)$, and $q_{\phi_\ell}(r_n)$, $n = 1, \dots, N$ by (6.2);
- Compute $\hat{\rho}(\phi_\ell)$ and $\hat{\zeta}(\phi_\ell)$ by (6.4);
- Compute $j(\phi_\ell) := \sum_{n=1}^{N} \left| g_{\phi_\ell}(r_n) - \hat{\rho}(\hat{\phi}_\ell)\, p_{\phi_\ell}(r_n) - \hat{\zeta}(\hat{\phi}_\ell)\, q_{\phi_\ell}(r_n) \right|^2$

end

Set $\hat{\phi}$ as minimizer of $j(\phi_\ell)$ over $\ell = 1, \dots, L$;

Output: Angular velocity $\boldsymbol{\omega}_t \approx \left(\hat{\rho}(\hat{\phi}) \cos \hat{\phi},\ \hat{\rho}(\hat{\phi}) \sin \hat{\phi},\ \hat{\zeta}(\hat{\phi}) \right)$.

Remark 6.1 The minimizer of $\mathcal{J}$ might not be unique in general, depending on the symmetry of the scattering potential f. In the described method, there are two steps of possible non-uniqueness: Firstly, the functions p_ϕ and q_ϕ might be linearly dependent, then the minimizer of $\mathcal{J}_\phi$ is not unique. Secondly, the subsequent minimization over $\phi \in [0, \pi)$ might lead to more than one minimum point. However, in our numerical tests below with non-symmetric functions f, we always computed approximately the correct minima.

Remark 6.2 If the object rotates around the origin without any further translation, i.e., $\boldsymbol{d}_t = \mathbf{0}$ for all t, then the function ν_t in Algorithms 1 and 2 for the common circle and infinitesimal common circle methods can be replaced by the complex-valued function μ_t from (5.2), where then the exponent in the phase factor vanishes.

Rotation matrix We compute rotation matrices R_t given angular velocities $\boldsymbol{\omega}_t$ for all $t \in (0, T)$. According to Theorem 4.3, we can obtain R_t from the angular velocity $\boldsymbol{\omega}_t$ with the corresponding coefficient matrix W_t by solving the initial value problem (4.7) which has a unique solution $R_t \in \mathrm{SO}(3)$ by [11, Section IV.4]. Numerically, we solve (4.7) with the forward *Euler method* on $\mathbb{R}^{3\times 3}$ followed by a so-called *retraction* P_{R_t}, see [1], which maps the tangential vectors from the tangent space $\{R_t S : S \in \mathbb{R}^{3\times 3} \text{ skew-symmetric}\}$ at $R_t \in \mathrm{SO}(3)$ to $\mathrm{SO}(3)$, in each iteration step. More precisely, using discrete time steps $t_j := j/n$ of resolution $n \in \mathbb{N}$, we compute for $j = 0, \dots, \lfloor Tn \rfloor$, the reconstructed rotation matrix $\mathbf{R}_j$ by

$$\begin{aligned} \mathbf{R}_0 &:= I, \\ \mathbf{R}_{j+1} &:= \mathrm{P}_{\mathbf{R}_j}((t_{j+1} - t_j)\, \mathbf{R}_j W_{t_j}). \end{aligned} \tag{6.6}$$

Since the manifold SO(3) is smooth and if we further assume the slightly higher regularity $R \in C^2([0,T] \to \mathrm{SO}(3))$, it is known that this method converges with the same order as the classical Euler method, see [11, Section IV.4]. The reconstruction is summarized in Algorithm 3.

Several retractions, that are computations of $\mathrm{P}_{\mathbf{R}_j}$, are possible in (6.6), see [1, Example 1.4.2], and we state two popular ones in the following. If a large number of computations is necessary, e.g., when training neural networks, the chosen method influences the computational time substantially, see [12].

(i) Polar decomposition: Starting with the singular value decomposition $A = U\Sigma V^\top$ of a matrix $A \in \mathbb{R}^{3\times 3}$ with diagonal matrix Σ and orthogonal matrices U and V, its polar decomposition is given by $A = \mathrm{Polar}(A)\tilde{\Sigma}$, where $\mathrm{Polar}(A) \coloneqq UV^\top$ and $\tilde{\Sigma} \coloneqq V\Sigma V^\top$. If $\det A > 0$, then $\mathrm{Polar}(A) \in \mathrm{SO}(3)$. It is well-known, see, e.g., [26], that $\mathrm{Polar}(A)$ is the orthogonal projection of A onto SO(3) with respect to the Frobenius norm $\|\cdot\|_F$, i.e., $\mathrm{Polar}(A) = \mathrm{argmin}_{Q\in\mathrm{SO}(3)} \|A - Q\|_F$. Hence a retraction is given by

$$\mathrm{P}_{\mathbf{R}_j}(\tilde{W}) = \mathrm{Polar}(\mathbf{R}_j + \tilde{W}). \tag{6.7}$$

(ii) Cayley transform: Based on the *Cayley transform*, a retraction is given for a skew-symmetric matrix $\tilde{W} \in \mathbb{R}^{3\times 3}$ by

$$\mathrm{P}_{\mathbf{R}_j}(\tilde{W}) = \mathbf{R}_j \,\mathrm{Cay}(\tilde{W}), \quad \text{where} \quad \mathrm{Cay}(\tilde{W}) \coloneqq (I - \tfrac{1}{2}\tilde{W})^{-1}(I + \tfrac{1}{2}\tilde{W}). \tag{6.8}$$

Algorithm 3: Reconstruction of the rotation matrices R_t with the infinitesimal method

Input: Angular velocity $\boldsymbol{\omega}_{t_j}$ on a grid $t_j = j/n$ for $j = 1, \dots, \lfloor Tn \rfloor$.
Set $\mathbf{R}_0 \coloneqq I$;
for $j = 0, \dots, \lfloor Tn \rfloor$ **do**
  Compute W_{t_j} by (4.2);
  Compute $\mathbf{R}_{j+1} \coloneqq \mathrm{P}_{\mathbf{R}_j}((t_{j+1} - t_j)\,\mathbf{R}_j W_{t_j})$, where $\mathrm{P}_{\mathbf{R}_j}$ is either (6.7) or (6.8);
end
Output: Rotation $R_{t_j} \approx \mathbf{R}_j$.

6.2 Reconstruction of the translations

The reconstruction of the translations $\boldsymbol{d}_t$ is based on Theorem 5.3. We assume that the rotations R_t are known from the section above. We numerically solve the nonlinear equations (5.3) and (5.4) for some $s, t \in [0,T]$ with the following approach.

The left-hand side of (5.3) is continuous with respect to β, and the term $\boldsymbol{\sigma}_{s,t}(\beta)$ in its exponent vanishes for $\beta = 0$. We couple the logarithm of (5.3) with a phase unwrapping [14], which selects the correct branch of the complex logarithm by imposing the continuity of the desired function. Note that the branches of the logarithm differ by adding $2\pi\mathrm{i}$. We obtain the linear system

$$\langle R_t\boldsymbol{d}_t - R_s\boldsymbol{d}_s, \boldsymbol{\sigma}_{s,t}(\beta)\rangle = \mathrm{unwrap}\left(\frac{1}{\mathrm{i}}\log\left(\frac{\mu_s(\boldsymbol{\gamma}_{s,t}(\beta))}{\mu_t(\boldsymbol{\gamma}_{t,s}(-\beta))}\right)\right), \qquad \beta \in J, \tag{6.9}$$

where unwrap denotes a phase unwrapping that vanishes at $\beta = 0$ and $J \subset J_{s,t}$ is an interval around 0 on which $\mu_s \circ \boldsymbol{\gamma}_{s,t}$ is nowhere zero. Discretizing the interval J, we see that (6.9) is a linear system of equations in $\boldsymbol{d}_{t;s}$. Analogously, we obtain from (5.4) the equation

$$\left\langle R_t\boldsymbol{d}_t - R_s\boldsymbol{d}_s, \boldsymbol{\sigma}^*_{s,t}(\beta)\right\rangle = \mathrm{unwrap}\left(\frac{1}{\mathrm{i}}\log\left(\frac{\mu_s(\boldsymbol{\gamma}^*_{s,t}(\beta))}{\mu_t(\boldsymbol{\gamma}^*_{t,s}(\beta))}\right)\right), \qquad \beta \in J. \tag{6.10}$$

If $s = 0$, we have $\boldsymbol{d}_0 = \mathbf{0}$ so that (6.9) and (6.10) contain as unknown only $\boldsymbol{d}_t$; then we reconstruct $\boldsymbol{d}_t$ as minimum norm solution fulfilling both (6.9) and (6.10). The procedure is summarized in Algorithm 4. Note that Lemma 5.1 guarantees a unique solution of the continuous problem. In order to improve the reconstruction for inexact data, we can also consider (6.9) and (6.10) for many pairs of s and t resulting in a large system of equation and solve for $\boldsymbol{d}_t$ for all t simultaneously, again incorporating $\boldsymbol{d}_0 = \mathbf{0}$.

Algorithm 4: Reconstruction of the translation $\boldsymbol{d}_t$

Input: Scaled squared energy μ_t from (5.1) and rotations R_t.
Set $\boldsymbol{d}_0 \coloneqq \mathbf{0}$;
for $j = 0, \dots, \lfloor Tn \rfloor$ **do**
  Compute $\boldsymbol{d}_{t_j}$ as the minimum norm least squares solution of both (6.9) and (6.10) with $s = 0$;
end
Output: Translations $\boldsymbol{d}_{t_j}$.

7 Numerical Simulations

We perform numerical tests of the reconstruction algorithms from Section 6. We compare the approaches of Sections 6.1.1 and 6.1.2 for the case that the motion depends smoothly on time. We consider two three-dimensional test functions for the scattering potential f, namely a cell phantom in Figure 6a, which consists of different convex and concave shapes with constant function values, and the Shepp–Logan phantom in Figure 6b. Both are evaluated on a uniform $N \times N \times N$ grid with $N = 160$ and they are not rotationally symmetric. Otherwise, any symmetry would cause the motion detection to have multiple solutions.

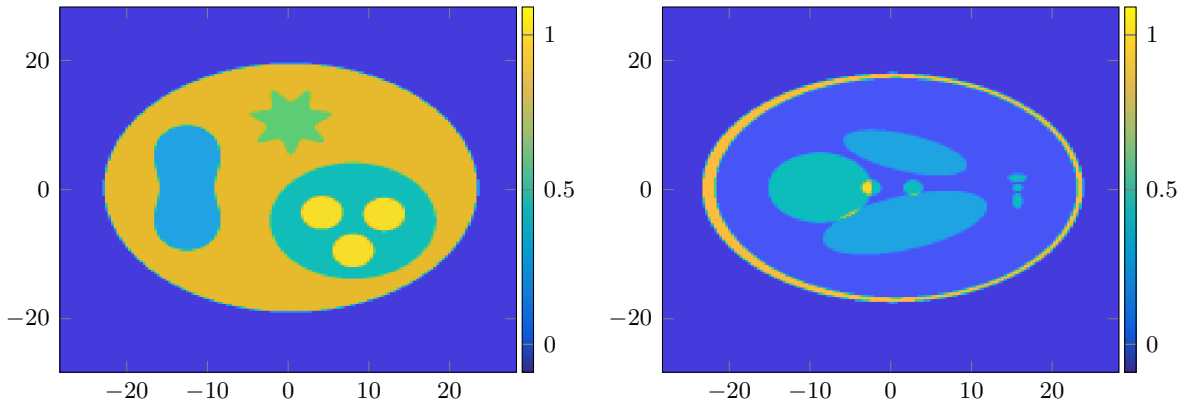

(a) Cell phantom

(b) Shepp–Logan phantom

Figure 6: Slice plots the 3D phantoms f at $x_3 = 0$.

The data ν_t is computed "in silico" via a numerical approximation of the Fourier transform $\mathcal{F}[f]$, where f is discretized on a finer grid of $(3N)^3 \approx 1.1 \cdot 10^8$ points. This approximation is done with the nonuniform fast Fourier transform (NFFT) algorithm [33], the same way as in [21]. We evaluate ν_t on a polar grid $(r\cos(\phi), r\sin(\phi))^\top$ on $\mathcal{B}^2_{k_0}$ consisting of $2N$ points in $r \in (-k_0, k_0)$ and $2N$ points of $\phi \in [0, \pi)$. We set the wave number $k_0 = 2\pi$, which corresponds to a wavelength of one of the incident wave. Furthermore, we have $4N = 640$ equispaced samples of the time $t \in [0, 2\pi)$. The high number of grid points yields in a good numerical approximation of the time-derivative. In total, we sample ν on about 65 million data points. We first consider the case that the object is only rotated, but not translated, then we utilize the complex-valued μ_t to reconstruct the rotation, see Remark 6.2.

Infinitesimal method Let $\mathbb{S}^2 := \{\boldsymbol{x} \in \mathbb{R}^2 : \|\boldsymbol{x}\| = 1\}$ denote the two-dimensional sphere. We first consider a constant rotation axis $\boldsymbol{n} \in \mathbb{S}^2$ and the rotation angle $t \in [0, 2\pi]$, that is, $R(t) = \exp(tN)$ with $N \in \mathbb{R}^{3\times 3}$ defined by $N\boldsymbol{x} = \boldsymbol{n} \times \boldsymbol{x}$ for all $\boldsymbol{x} \in \mathbb{R}^3$, since we then have, according to Rodrigues' rotation formula, $R(t)\boldsymbol{x} = \langle \boldsymbol{n}, \boldsymbol{x}\rangle\, \boldsymbol{n} + \sin(t)\boldsymbol{n} \times \boldsymbol{x} + \cos(t)(\boldsymbol{n} \times \boldsymbol{x}) \times \boldsymbol{n}$ for all $\boldsymbol{x} \in \mathbb{R}^3$. The angular velocity is in this case therefore the constant function $\boldsymbol{\omega}_t = \boldsymbol{n}$. In Figure 7, we show the misfit functional j from (6.5) for the rotation axis $\boldsymbol{n} = (0.96\cos(\pi/4), 0.96\sin(\pi/4), 0.28)^\top$ at the time $t = \pi/4$. One can clearly spot the expected minimum of j at $\hat{\phi} = \pi/4$. Furthermore, we show in Figure 8 the error of the angular velocity reconstructed with Algorithm 2 for all time steps t corresponding to a full turn of the object. We note that the radius ρ_t has a higher error than the other components.

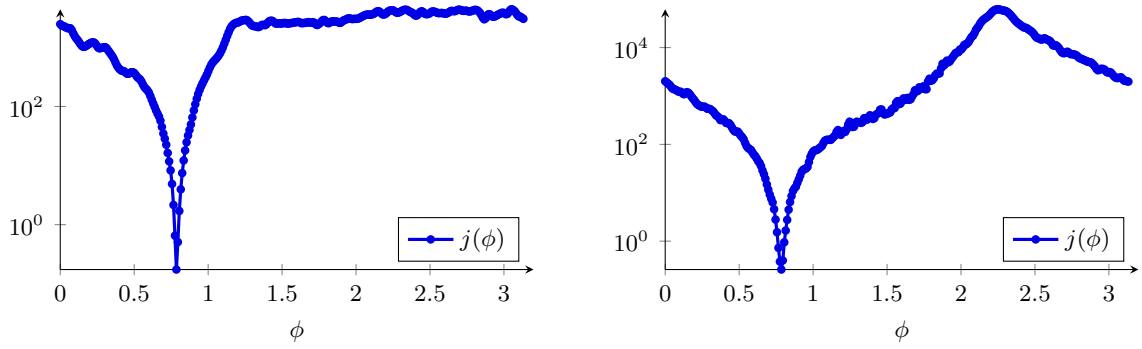

Figure 7: Plot of the function j for time step $t = \pi/4$. *Left:* cell phantom, *right:* Shepp–Logan.

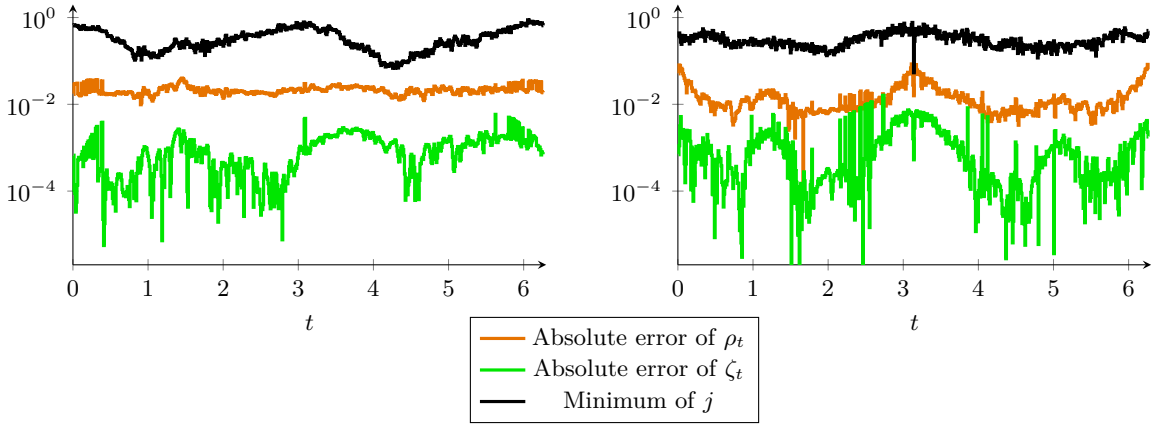

Figure 8: Absolute error of the components (4.3) of the angular velocity $\boldsymbol{\omega}_t$ and the minimum of the functional j_t, depending on t. The reconstructed value for ϕ_t takes only values on the grid, and in this case it is reconstructed exactly; note that the true value is also on the grid. *Left:* cell phantom, *right:* Shepp–Logan phantom.

Inserting the reconstructed angular velocity, we apply Algorithm 3 to obtain the rotation matrices. The reconstructions are denoted as $\mathbf{R}_t^{\mathrm{Pol}}$ with the polar decomposition (6.7), and $\mathbf{R}_t^{\mathrm{Cay}}$ with the Cayley transform (6.8) as retraction. The resulting error, measured in the Frobenius norm, is shown in Figure 9, where we see that both retractions perform almost equally.

Remark 7.1 (Sampling) Here, we assume that ν_t is given on a polar grid in order to easily compute the derivatives in (6.2), which we approximate numerically by central differences on the polar grid. However, the numerical reconstruction of f for known rotations seems to be a little worse than with a uniform, rectangular grid for ν_t as considered in [21]. However, the actual experiment takes measurements of the scattered wave u_t. Then ν_t is related to u_t via a 2D Fourier transform in (3.1). It seems natural that the images of u_t are captured on a uniform grid. A canonical discretization of (3.1) is the fast Fourier transform, which gives an approximation of

ν_t on a uniform grid, cf. [2]. Nevertheless, the nonuniform fast Fourier transform [29, Section 7] can be used to evaluate ν_t accurately on any set such as a polar grid.

Combination of the infinitesimal with the direct common circle method The error of the reconstruction in Figure 9 based on the infinitesimal method grows with the time t. This behavior is quite expected since we make a small error in each time step and the errors accumulate. In order to get a better reconstruction, we use the direct common circle method in Algorithm 1. We minimize the functional $\mathcal{E}_{s,t}$, given in (6.1), over SO(3) iteratively with the Nelder–Mead downhill simplex method [24] implemented in Matlab's `fminsearch` routine, which does not require derivatives. As starting solution, where we insert the Euler angles of $\mathbf{R}_t^{\mathrm{Cay}}$ reconstructed with the infinitesimal method as above. The evaluation of ν_t, which is sampled on a polar grid, at the curves $\boldsymbol{\gamma}^{\varphi,\theta}$ utilizes cubic spline interpolation. The error of the reconstruction with this combined approach is shown in Figure 9. We see that the reconstruction greatly benefits from the combined approach.

Furthermore, we have noticed that taking a random starting solution for the optimization of (6.1) often yields very bad results, since $\mathcal{E}_{s,t}$ might have multiple local minima. A possible approach would consist in evaluating $\mathcal{E}_{s,t}$ on a grid in $\mathbb{R}^3$ and taking the minimum or by using multiple random starting solutions. However, this seems unnecessary, since we can rely on the good starting solution obtained with the infinitesimal method.

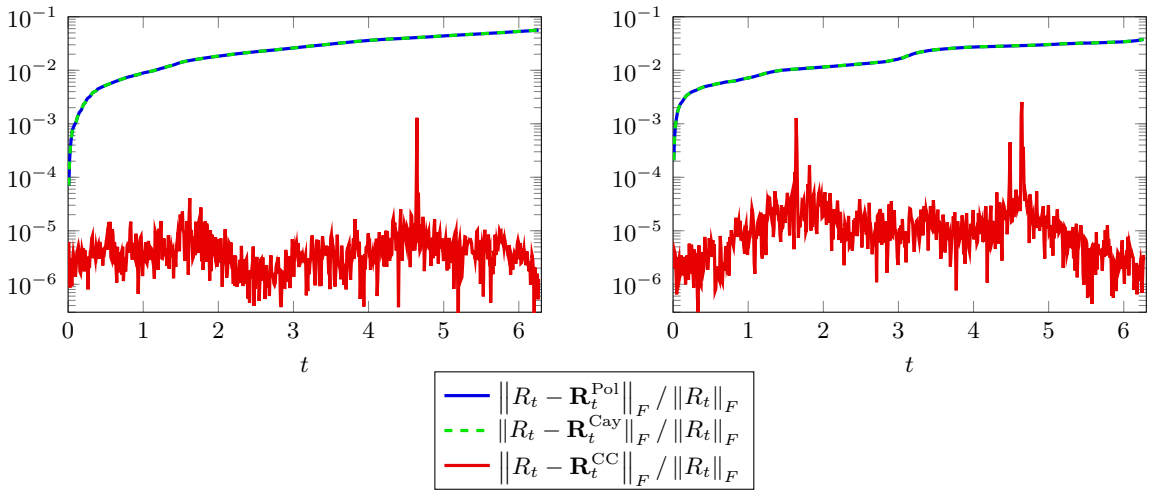

Figure 9: Relative error of the reconstructed rotation matrices $\mathbf{R}_t^{\mathrm{Pol}}$ and $\mathbf{R}_t^{\mathrm{Cay}}$ using Euler's method (6.6) with the polar decomposition (6.7) or the Cayley transform (6.8), respectively. Furthermore, R_t^{CC} refers to the rotation matrix reconstructed with the minimization of (6.1) to find the common circles, where the starting solution of the optimization was in each step computed with the infinitesimal method and the Cayley transform as above. *Left:* cell phantom, *right:* Shepp–Logan phantom.

Moving rotation axis In our next simulation, we consider the time-dependent rotation axis $\boldsymbol{n}(t) = (\sqrt{1-a^2}\cos(b\,\sin(t/2)), \sqrt{1-a^2}\sin(b\,\sin(t/2)), a)^\top \in \mathbb{S}^2$ for $a = 0.28$ and $b = 0.5$. The obtained error is shown in Figure 10. Overall, the results are similar to the ones for the constant rotation axis. However, there is a larger error around $t \approx 0$, which might be explained by the fact that for a small rotation the respective hemispheres and thus also the data ν_t and ν_0 are very close together, which makes detecting the common circles harder. This could be circumvented by applying the common circles method to rotations that are farther apart. A similar observation was made that the common lines in context of the ray transform also become harder to detect in case of very small rotations where the infinitesimal method suits better, see [8].

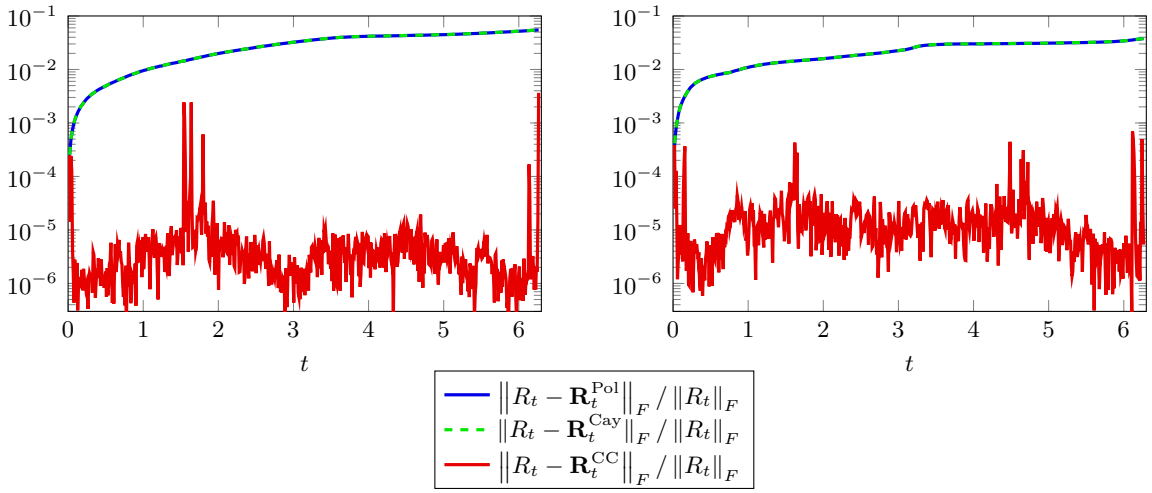

Figure 10: Relative error of the rotation matrix R_t, reconstructed using the same setup and methods as in Figure 9, but with a moving rotation axis.

Reconstruction of the translation Now, we consider the case that the object also moves according to the translation $\boldsymbol{d}_t = 4(\sin t, \sin t, \sin t)^\top$, $t \in [0, 2\pi]$, and the rotation is the same as in the previous example with the moving axis. We first reconstruct the rotations with the same methods as above. Afterwards, we recover the translations $\boldsymbol{d}_t$ by Algorithm 4. The reconstruction error is shown in Figure 11, where we see that the translation is reconstructed quite reliably. The error of the rotation is larger than in the case without translation, but it is still on an acceptable level. This is because we could only use the real-valued ν_t for reconstructing the rotations as the translations do not vanish, cf. Remark 6.2. Especially for large translations, we have noted in the simulations that the unwrapping in (6.9) does not always yield good results because of the inexactness of the data. This could be mitigated by combining it with a nonlinear optimization directly applied to (5.3) and (5.4).

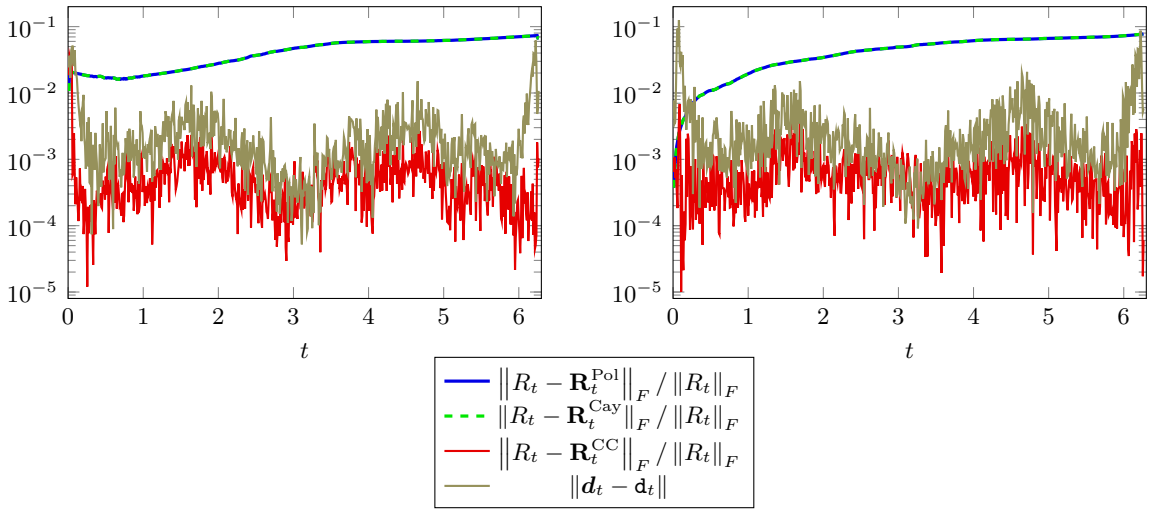

Figure 11: Error of the reconstructed rotation matrix and reconstructed translation $\mathtt{d}_t$, for the case of a non-zero translation. Note that $\|\boldsymbol{d}_t\|$ varies between 0 and approximately 6.9, so it does not make sense to compute relative errors. *Left:* cell phantom, *Right:* Shepp–Logan phantom.

Finally, we show in Figure 12 the reconstructed images of the scattering potential f, where we have first computed the rotations and translations with the above combined common circle method for the moving rotation axis. In the second part, i.e., the image reconstruction with

known motion, we use the nonuniform Fourier reconstruction technique from [21]. For the image reconstruction, we evaluate μ_t on a uniform grid instead of the polar grid used for the common circle method, since the reconstruction of the image f for a polar grid shows an inferior quality. This observation is consistent with numerical evidence in [10], which showed that an approximate inversion of discrete Fourier transforms on a two-dimensional polar grid often shows large errors even for a very large number of sampling points.

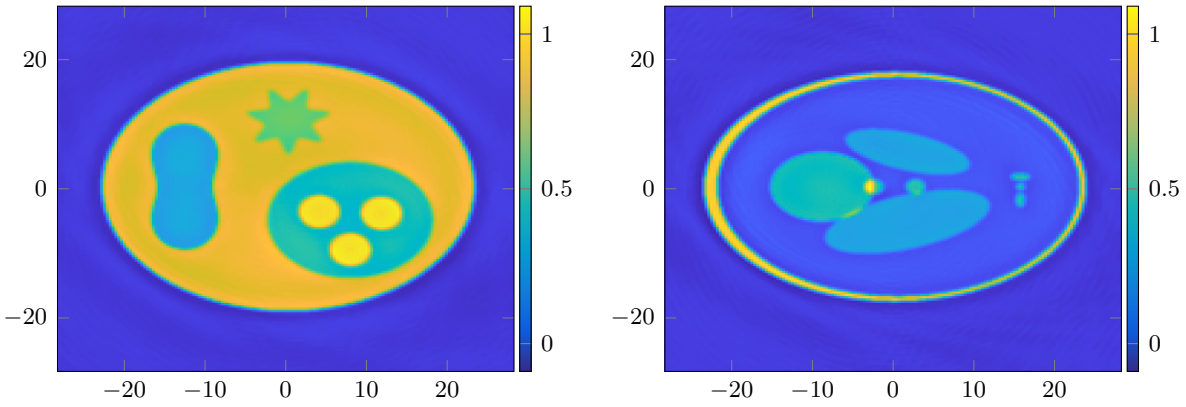

(a) Cell phantom (PSNR 32.21, SSIM 0.754)

(b) Shepp–Logan (PSNR 30.85, SSIM 0.772)

Figure 12: Slice plots of the reconstructed scattering potential f, where the rotation and translation was estimated with the common circle method as in Figure 11. The image quality is assessed via the peak signal-to-noise ratio (PSNR) and the structural similarity index (SSIM).

Computational time The numerical simulations were performed with Matlab on a standard PC with an 8-core Intel i7-10700 processor and 32 GB of memory. We utilized the NFFT software package [19, 18] for the Fourier transforms. The reconstruction of the motion parameters for all 640 time steps as in Figure 11 took about 40 seconds. The image reconstruction in Figure 12 took about 90 seconds.

8 Conclusions

In this paper, we have considered the reconstruction of the motion of an object in diffraction tomography. For the reconstruction of the rotation, we have presented a common circle method and its infinitesimal version. While the former method usually produced more accurate results, it benefits from using a starting solution with the computationally faster infinitesimal approach. Furthermore, we have shown that also the translation of the object can be uniquely recovered from the diffraction data. For this, we have required that the scattering potential is real-valued. We note that, in contrast to projection images corresponding to the ray transform, also the position and orientation of the object in direction of the incident wave can be detected here.

Future research will focus on the real-world application related to optical diffraction tomography with acoustical tweezers. Furthermore, we intend to incorporate phase retrieval methods for the motion detection since often only the intensities of the field $u^{\mathrm{sca}} + u^{\mathrm{inc}}$ can be measured.

Acknowledgments

Funding by the DFG under the SFB “Tomography Across the Scales” (STE 571/19-1, project number: 495365311) is gratefully acknowledged. Moreover, PE and OS are supported by the Austrian Science Fund (FWF), with SFB F68 “Tomography Across the Scales”, project F6804-N36 and F6807-N36. The financial support by the Austrian Federal Ministry for Digital and

Economic Affairs, the National Foundation for Research, Technology and Development and the Christian Doppler Research Association is gratefully acknowledged. This research was funded in whole, or in part, by the Austrian Science Fund (FWF) P 34981. For the purpose of open access, the authors have applied a CC BY public copyright license to any Authors Accepted Manuscript version arising from this submission.

References

[1] P.-A. Absil, R. Mahony, and R. Sepulchre. *Optimization Algorithms on Matrix Manifolds*. Princeton University Press, 2008.

[2] R. Beinert and M. Quellmalz. Total variation-based reconstruction and phase retrieval for diffraction tomography. *SIAM Journal on Imaging Sciences*, 15(3):1373–1399, 2022.

[3] T. Bendory, A. Bartesaghi, and A. Singer. Single-particle cryo-electron microscopy: Mathematical theory, computational challenges, and opportunities. *IEEE Signal Processing Magazine*, 37(2):58–76, 2020.

[4] G. Bortel and M. Tegze. Common arc method for diffraction pattern orientation. *Acta Cryst.*, A67:533–543, 2011.

[5] D. Colton and R. Kress. *Inverse Acoustic and Electromagnetic Scattering Theory*. Number 93 in Applied Mathematical Sciences. Springer, Berlin, 3rd edition, 2013.

[6] A. Devaney. A filtered backpropagation algorithm for diffraction tomography. *Ultrasonic Imaging*, 4(4):336–350, 1982.

[7] K. Dholakia, B. W. Drinkwater, and M. Ritsch-Marte. Comparing acoustic and optical forces for biomedical research. *Nature Reviews Physics*, 2(9):480–491, 2020.

[8] P. Elbau, M. Ritsch-Marte, O. Scherzer, and D. Schmutz. Motion reconstruction for optical tomography of trapped objects. *Inverse Problems*, 36(4):044004, 2020.

[9] F. Faucher, C. Kirisits, M. Quellmalz, O. Scherzer, and E. Setterqvist. Diffraction tomography, Fourier reconstruction, and full waveform inversion. In K. Chen, C.-B. Schönlieb, X.-C. Tai, and L. Younes, editors, *Handbook of Mathematical Models and Algorithms in Computer Vision and Imaging*, pages 273–312. Springer, Cham, 2023.

[10] M. Fenn, S. Kunis, and D. Potts. On the computation of the polar FFT. *Applied and Computational Harmonic Analysis*, 22:257–263, 2007.

[11] E. Hairer, C. Lubich, and G. Wanner. *Geometric Numerical Integration*, volume 31 of *Springer Series in Computational Mathematics*. Springer, Berlin, 2nd edition, 2006.

[12] M. Hasannasab, J. Hertrich, S. Neumayer, G. Plonka, S. Setzer, and G. Steidl. Parseval proximal neural networks. *Journal of Fourier Analysis and Applications*, 26(59):1–31, 2020.

[13] G. Huldt, A. Szőke, and J. Hajdu. Diffraction imaging of single particles and biomolecules. *J. Struct. Biol.*, 144(1):219–227, 2003.

[14] K. Itoh. Analysis of the phase unwrapping problem. *Applied Optics*, 21(14), 1982.

[15] P. H. Jones, O. M. Maragò, and G. Volpe. *Optical Tweezers*. Cambridge University Press, Cambridge, 2015.

[16] A. C. Kak and M. Slaney. *Principles of Computerized Tomographic Imaging*. Number 33 in Classics in Applied Mathematics. Society for Industrial and Applied Mathematics (SIAM), Philadelphia, PA, 2001. Reprint of the 1988 original.

[17] Z. Kam. The reconstruction of structure from electron micrographs of randomly oriented particles. *Journal of Theoretical Biology*, 82(1):15–39, 1980.

[18] J. Keiner, S. Kunis, and D. Potts. NFFT 3.5, C subroutine library. https://www.tu-chemnitz.de/~potts/nfft. Contributors: F. Bartel, M. Fenn, T. Görner, M. Kircheis, T. Knopp, M. Quellmalz, M. Schmischke, T. Volkmer, A. Vollrath.

[19] J. Keiner, S. Kunis, and D. Potts. Using NFFT3 - a software library for various nonequispaced fast Fourier transforms. *ACM Transactions on Mathematical Software*, 36:Article 19,1–30, 2009.

[20] J. Ketola and L. Lamberg. An algorithm for recovering unknown projection orientations and shifts in 3-d tomography. *Inverse Problems and Imaging*, 5(1):75–93, 2011.

[21] C. Kirisits, M. Quellmalz, M. Ritsch-Marte, O. Scherzer, E. Setterqvist, and G. Steidl. Fourier reconstruction for diffraction tomography of an object rotated into arbitrary orientations. *Inverse Problems*, 37(11):115002, 2021.

[22] P. Kurlberg and G. Zickert. Formal uniqueness in Ewald sphere corrected single particle analysis. *ArXiv 2104.05371*, 2021.

[23] M. Kvåle Løvmo, B. Pressl, G. Thalhammer, and M. Ritsch-Marte. Controlled orientation and sustained rotation of biological samples in a sono-optical microfluidic device. *Lab on a Chip*, 21(8):1563–1578, 2021.

[24] J. C. Lagarias, J. A. Reeds, M. H. Wright, and P. E. Wright. Convergence properties of the Nelder–Mead simplex method in low dimensions. *SIAM Journal on Optimization*, 9(1):112–147, 2009.

[25] L. D. Landau and E. M. Lifshitz. *Mechanics*, volume 1 of *Course of Theoretical Physics*. Butterworth–Heinemann, Oxford, 3rd edition, 1981.

[26] M. Moakher. Means and averaging in the group of rotations. *SIAM Journal on Matrix Analysis and Applications*, 24(1):1–16, 2002.

[27] P. Müller, M. Schürmann, and J. Guck. The theory of diffraction tomography, 2015. ArXiv 1507.00466v3.

[28] F. Natterer and F. Wübbeling. *Mathematical Methods in Image Reconstruction*. Number 5 in Monographs on Mathematical Modeling and Computation. SIAM, Philadelphia, PA, 2001.

[29] G. Plonka, D. Potts, G. Steidl, and M. Tasche. *Numerical Fourier Analysis*. Applied and Numerical Harmonic Analysis. Birkhäuser, Cham, 2018.

[30] D. Schmutz. Reconstruction of projection orientations in cryo-electron microscopy, 2017. Master's thesis, University of Vienna.

[31] N. Sharon, J. Kileel, Y. Khoo, B. Landa, and A. Singer. Method of moments for 3d single particle ab initio modeling with non-uniform distribution of viewing angles. *Inverse Problems*, 36(4):044003, 2020.

[32] A. Singer, R. R. Coifman, F. J. Sigworth, D. W. Chester, and Y. Shkolnisky. Detecting consistent common lines in cryo-EM by voting. *Journal of Structural Biology*, 169(3):312–322, 2010.

[33] G. Steidl. A note on fast Fourier transforms for nonequispaced grids. *Advances in Computational Mathematics*, 9(3-4):337–353, 1998.

[34] G. Thalhammer, R. Steiger, M. Meinschad, M. Hill, S. Bernet, and M. Ritsch-Marte. Combined acoustic and optical trapping. *Biomedical Optics Express*, 2(10):2859–2870, 2011.

[35] M. van Heel. Angular reconstitution: A posteriori assignment of projection directions for 3d reconstruction. *Ultramicroscopy*, 21(2):111–123, 1987.

[36] M. van Heel, B. Gowen, R. Matadeen, E. V. Orlova, R. Finn, T. Pape, D. Cohen, H. Stark, R. Schmidt, M. Schatz, and A. Patwardhan. Single-particle electron cryo-microscopy: towards atomic resolution. *Quarterly Reviews of Biophysics*, 33(4):307–369, 2000.

[37] L. Wang, A. Singer, and Z. Wen. Orientation determination of cryo-EM images using least unsquared deviations. *SIAM Journal on Imaging Sciences*, 6(4):2450–2483, 2013.

[38] E. Wolf. Three-dimensional structure determination of semi-transparent objects from holographic data. *Optics Communications*, 1:153–156, 1969.

A Proofs of Section 3

Proof (of Lemma 3.1): By (3.5), a point $\boldsymbol{x} \in \mathbb{R}^3$ is in the intersection $\mathcal{H}_s \cap \mathcal{H}_t$ if and only if it fulfills the equations

$$\left\|\boldsymbol{x} + k_0 R_s \boldsymbol{e}^3\right\|^2 = k_0^2 \quad \text{and} \quad \left\|\boldsymbol{x} + k_0 R_t \boldsymbol{e}^3\right\|^2 = k_0^2 \tag{A.1}$$

and the two inequalities

$$\langle \boldsymbol{x}, R_s \boldsymbol{e}^3 \rangle > -k_0 \quad \text{and} \quad \langle \boldsymbol{x}, R_t \boldsymbol{e}^3 \rangle > -k_0. \tag{A.2}$$

Taking their sum and their difference, the two equations (A.1) are seen to be equivalent to

$$\left\|\boldsymbol{x} + \frac{k_0}{2}(R_s \boldsymbol{e}^3 + R_t \boldsymbol{e}^3)\right\|^2 = \frac{k_0^2}{4}\left\|R_s \boldsymbol{e}^3 + R_t \boldsymbol{e}^3\right\|^2 \quad \text{and} \quad \langle \boldsymbol{x}, R_s \boldsymbol{e}^3 - R_t \boldsymbol{e}^3 \rangle = 0,$$

meaning that $\boldsymbol{x}$ is on a circle with radius $a_{s,t}$ around the point $-a_{s,t}\boldsymbol{v}_{s,t}^1$ in the subspace $\mathcal{V}_{s,t}$ spanned by the vectors $\boldsymbol{v}_{s,t}^1$ and $\boldsymbol{v}_{s,t}^2$, so that we can write

$$\boldsymbol{x} = a_{s,t}(\cos(\beta) - 1)\boldsymbol{v}_{s,t}^1 + a_{s,t}\sin(\beta)\boldsymbol{v}_{s,t}^2 \quad \text{for some} \quad \beta \in (-\pi, \pi].$$

For such a point $\boldsymbol{x}$, the two inequalities (A.2) are equivalent and reduce to the condition

$$\frac{k_0}{2}(\cos(\beta) - 1)(1 + \langle R_s \boldsymbol{e}^3, R_t \boldsymbol{e}^3 \rangle) > -k_0, \quad \text{that is,} \quad \cos(\beta) > \frac{\langle R_s \boldsymbol{e}^3, R_t \boldsymbol{e}^3 \rangle - 1}{\langle R_s \boldsymbol{e}^3, R_t \boldsymbol{e}^3 \rangle + 1}$$

for the variable β. □

Proof (of Lemma 3.2): Since $R_s\boldsymbol{h}$ is a parameterization of $\mathcal{H}_s$ and $\boldsymbol{h}$ restricted to its first two components is just the identity, we can solve the relation $R_s\boldsymbol{h}(\boldsymbol{k}) = \boldsymbol{x}$ for every $\boldsymbol{x} \in \mathcal{H}_s$ by orthogonally projecting $R_s^\top \boldsymbol{x}$ onto its first two components

$$\boldsymbol{k} = P(R_s^\top \boldsymbol{x}).$$

Therefore we find directly from the representation (3.6) of $\mathcal{H}_s \cap \mathcal{H}_t$ that

$$\boldsymbol{\gamma}_{s,t}(\beta) = a_{s,t}(\cos(\beta) - 1)P(R_s^\top \boldsymbol{v}_{s,t}^1) + a_{s,t}\sin(\beta)P(R_s^\top \boldsymbol{v}_{s,t}^2). \tag{A.3}$$

Further we get for the projections of the basis vectors

$$\begin{aligned} P(R_s^\top \boldsymbol{v}_{s,t}^1) &= \frac{P(\boldsymbol{e}^3 + R_s^\top R_t \boldsymbol{e}^3)}{\|R_s\boldsymbol{e}^3 + R_t\boldsymbol{e}^3\|} = \frac{\tilde{a}_{s,t}}{a_{s,t}}\boldsymbol{w}_{s,t}^1 \quad \text{and} \\ P(R_s^\top \boldsymbol{v}_{s,t}^2) &= \frac{P(\boldsymbol{e}^3 \times R_s^\top R_t \boldsymbol{e}^3)}{\|R_s\boldsymbol{e}^3 \times R_t\boldsymbol{e}^3\|} = \boldsymbol{w}_{s,t}^2, \end{aligned} \tag{A.4}$$

so that the equation (A.3) for $\boldsymbol{\gamma}_{s,t}$ becomes (3.9). □

Proof (of Proposition 3.3): We have that

$$R_s^\top R_t \boldsymbol{e}^3 = Q^{(3)}(\varphi)Q^{(2)}(\theta)Q^{(3)}(\psi)\boldsymbol{e}^3 = Q^{(3)}(\varphi)Q^{(2)}(\theta)\boldsymbol{e}^3 = \begin{pmatrix} \cos(\varphi)\sin(\theta) \\ \sin(\varphi)\sin(\theta) \\ \cos(\theta) \end{pmatrix}.$$

Plugging this into $\boldsymbol{\gamma}_{s,t}$ from (3.9), we find for the lengths of the semi-axes

$$\begin{aligned} \tilde{a}_{s,t} &= \frac{k_0}{2}\left\|P(R_s^\top R_t \boldsymbol{e}^3)\right\| = \frac{k_0}{2}\sin(\theta) \quad \text{and} \\ a_{s,t} &= \frac{k_0}{2}\left\|R_s\boldsymbol{e}^3 + R_t\boldsymbol{e}^3\right\| = \frac{k_0}{2}\left\|\boldsymbol{e}^3 + R_s^\top R_t \boldsymbol{e}^3\right\| = \frac{k_0}{2}\sqrt{2 + 2\cos(\theta)} = k_0\cos(\tfrac{\theta}{2}); \end{aligned}$$

and for the directions of the semi-axes $\boldsymbol{w}_{s,t}^1 = \begin{pmatrix} \cos(\varphi) \\ \sin(\varphi) \end{pmatrix}$ and $\boldsymbol{w}_{s,t}^2 = \begin{pmatrix} -\sin(\varphi) \\ \cos(\varphi) \end{pmatrix}$. □

Proof (of Proposition 3.4): The proof goes along the same lines as Lemma 3.1, Lemma 3.2, and Proposition 3.3.

(i) By replacing $R_t\boldsymbol{e}^3$ by $-R_t\boldsymbol{e}^3$ in Lemma 3.1, we directly get the parameterization $\boldsymbol{\sigma}_{s,t}^*$ of $\mathcal{H}_s \cap (-\mathcal{H}_t)$ in the form of (3.14).

(ii) Proceeding as in Lemma 3.2, we find the curve $\boldsymbol{\gamma}_{s,t}^*$ by

$$\boldsymbol{\gamma}_{s,t}^*(\beta) = P(R_s^\top \boldsymbol{\sigma}_{s,t}^*(\beta)) = a_{s,t}^*(\cos(\beta) - 1)P(R_s^\top \boldsymbol{v}_{s,t}^3) - a_{s,t}^*\sin(\beta)P(R_s^\top \boldsymbol{v}_{s,t}^2).$$

With

$$P(R_s^\top \boldsymbol{v}_{s,t}^3) = \frac{P(\boldsymbol{e}^3 - R_s^\top R_t \boldsymbol{e}^3)}{\|R_s\boldsymbol{e}^3 - R_t\boldsymbol{e}^3\|} = -\frac{k_0}{2}\frac{P(R_s^\top R_t \boldsymbol{e}^3)}{a_{s,t}^*} = -\frac{\tilde{a}_{s,t}}{a_{s,t}^*}\boldsymbol{w}_{s,t}^1, \tag{A.5}$$

this yields the equation (3.16) for $\boldsymbol{\gamma}_{s,t}^*$.

(iii) Taking finally the expressions of $\tilde{a}_{s,t}$, $\boldsymbol{w}_{s,t}^1$, and $\boldsymbol{w}_{s,t}^2$ in terms of the Euler angles of $R_s^\top R_t$ from the proof of Proposition 3.3, we obtain with

$$a_{s,t}^* := \frac{k_0}{2}\left\|\boldsymbol{e}^3 - R_s^\top R_t \boldsymbol{e}^3\right\| = \frac{k_0}{2}\sqrt{2 - 2\cos(\theta)} = k_0\sin(\tfrac{\theta}{2})$$

the identity in (3.17). □

Proof (of Proposition 3.5): (i) Since $R_s^\top R_t e^3 = e^3$, the rotation $R_s^\top R_t$ has the rotation axis e^3 and is therefore of the form $R_s^\top R_t = Q^{(3)}(\alpha)$ for some $\alpha \in \mathbb{R}/(2\pi\mathbb{Z})$. Then, we see from the definition (2.5) of $\boldsymbol{h}$ that we have for all $\boldsymbol{k} \in \mathcal{B}^2_{k_0}$

$$R_s^\top R_t \boldsymbol{h}(\boldsymbol{k}) = Q^{(3)}(\alpha)\boldsymbol{h}(\boldsymbol{k}) = \boldsymbol{h}(\mathrm{Q}(\alpha)\boldsymbol{k}) \tag{A.6}$$

and therefore, according to (3.2),

$$\nu_s(\mathrm{Q}(\alpha)\boldsymbol{k}) = |\mathcal{F}[f](R_s\boldsymbol{h}(\mathrm{Q}(\alpha)\boldsymbol{k}))|^2 = |\mathcal{F}[f](R_t\boldsymbol{h}(\boldsymbol{k}))|^2 = \nu_t(\boldsymbol{k}).$$

(ii) Since $Q^{(2)}(\pi)R_s^\top R_t e^3 = -Q^{(2)}(\pi)e^3 = e^3$, the rotation $Q^{(2)}(\pi)R_s^\top R_t$ has the rotation axis e^3 and we therefore have $R_s^\top R_t = Q^{(2)}(\pi)Q^{(3)}(\alpha)$ for some $\alpha \in \mathbb{R}/(2\pi\mathbb{Z})$. Then, we see from the definition (2.5) of $\boldsymbol{h}$ that we have for all $\boldsymbol{k} \in \mathcal{B}^2_{k_0}$

$$R_s^\top R_t \boldsymbol{h}(\boldsymbol{k}) = Q^{(2)}(\pi)Q^{(3)}(\alpha)\boldsymbol{h}(\boldsymbol{k}) = Q^{(2)}(\pi)\boldsymbol{h}(\mathrm{Q}(\alpha)\boldsymbol{k}) = -\boldsymbol{h}(\mathrm{SQ}(\alpha)\boldsymbol{k}) \tag{A.7}$$

and therefore, according to (3.2) and (3.13),

$$\nu_s(\mathrm{SQ}(\alpha)\boldsymbol{k}) = |\mathcal{F}[f](R_s\boldsymbol{h}(S\mathrm{Q}(\alpha)\boldsymbol{k}))|^2 = |\mathcal{F}[f](-R_t\boldsymbol{h}(\boldsymbol{k}))|^2 = |\mathcal{F}[f](R_t\boldsymbol{h}(\boldsymbol{k}))|^2 = \nu_t(\boldsymbol{k}). \qquad \square$$

Proof (of Theorem 3.6): According to Proposition 3.5, the fact that neither $\nu_s(\mathrm{Q}(\alpha)\boldsymbol{k}) = \nu_t(\boldsymbol{k})$ nor $\nu_s(\mathrm{SQ}(\alpha)\boldsymbol{k}) = \nu_t(\boldsymbol{k})$ holds for all $\boldsymbol{k} \in \mathcal{B}^2_{k_0}$ for any choice of parameter $\alpha \in \mathbb{R}/(2\pi\mathbb{Z})$ excludes the cases where $R_s e^3 = \pm R_t e^3$ and we can find the elliptic arcs $\boldsymbol{\gamma}_{s,t}$ and $\boldsymbol{\gamma}_{t,s}$ and the dual arcs $\boldsymbol{\gamma}^*_{s,t}$ and $\boldsymbol{\gamma}^*_{t,s}$ as in Lemma 3.2 and Proposition 3.4.

We parameterize the matrix $R_s^\top R_t$ in Euler angles $(\tilde\varphi, \tilde\theta, \tilde\psi) \in (\mathbb{R}/(2\pi\mathbb{Z})) \times [0,\pi] \times (\mathbb{R}/(2\pi\mathbb{Z}))$ as in (3.11). Then, the representation of the transposed matrix $R_t^\top R_s$ in Euler angles is given by

$$R_t^\top R_s = (R_s^\top R_t)^\top = Q^{(3)}(-\tilde\psi)Q^{(2)}(-\tilde\theta)Q^{(3)}(-\tilde\varphi) = Q^{(3)}(\pi-\tilde\psi)Q^{(2)}(\tilde\theta)Q^{(3)}(\pi-\tilde\varphi), \tag{A.8}$$

where we used the identity $Q^{(2)}(-\tilde\theta) = Q^{(3)}(\pi)Q^{(2)}(\tilde\theta)Q^{(3)}(\pi)$ to shift the angles for $R_t^\top R_s$ into the chosen area of definition. By (3.12), we see that $\boldsymbol{\gamma}^{\tilde\varphi,\tilde\theta} = \boldsymbol{\gamma}_{s,t}$ and $\boldsymbol{\gamma}^{\pi-\tilde\psi,\tilde\theta} = \boldsymbol{\gamma}_{t,s}$, and by (3.17) that $\boldsymbol{\gamma}^{*,\tilde\varphi,\tilde\theta} = \boldsymbol{\gamma}^*_{s,t}$ and $\boldsymbol{\gamma}^{*,\pi-\tilde\psi,\tilde\theta} = \boldsymbol{\gamma}^*_{t,s}$. Since the curves $\boldsymbol{\gamma}_{s,t}$ and $\boldsymbol{\gamma}_{t,s}$ as well as $\boldsymbol{\gamma}^*_{s,t}$ and $\boldsymbol{\gamma}^*_{t,s}$ fulfill by construction the equations (3.10) and (3.18), and $\boldsymbol{\gamma}^{\varphi,\theta}$, $\boldsymbol{\gamma}^{\pi-\psi,\theta}$, $\boldsymbol{\gamma}^{*,\varphi,\theta}$, and $\boldsymbol{\gamma}^{*,\pi-\psi,\theta}$ are by assumption the only elliptic arcs of this form fulfilling (3.22) and (3.23), we have that $\varphi = \tilde\varphi$, $\theta = \tilde\theta$, and $\psi = \tilde\psi$, which implies (3.24). We note that the two pairs of curves can in general not be interchanged because in (3.22) the curve $\boldsymbol{\gamma}^{\varphi,\theta}(\cdot)$ is traversed conter-clockwise while $\boldsymbol{\gamma}^{\pi-\psi,\theta}(-\cdot)$ is traversed clockwise, whereas in (3.23) both $\boldsymbol{\gamma}^{*,\varphi,\theta}$ and $\boldsymbol{\gamma}^{*,\pi-\psi,\theta}$ are traversed counter-clockwise. $\square$

B Proof of Lemma 4.1

Proof: We define the continuously differentiable function $H\colon [0,T] \times \mathcal{B}^2_{k_0} \to \mathbb{R}^3$ by $H(t,\boldsymbol{k}) \coloneqq R_t\boldsymbol{h}(\boldsymbol{k})$ with $\boldsymbol{h}$ being the parameterization from (2.5). By the definition (4.1) of the angular velocity $\boldsymbol{\omega}_t$, we have $R_t'\boldsymbol{k} = R_t(\boldsymbol{\omega}_t \times \boldsymbol{k})$. Then for the partial derivative of H with respect to the first argument t at the point $\boldsymbol{k} = r\boldsymbol{\phi}_t$ reads

$$\partial_t H(t, r\boldsymbol{\phi}_t) = R_t'\,\boldsymbol{h}(r\boldsymbol{\phi}_t) = R_t(\boldsymbol{\omega}_t \times \boldsymbol{h}(r\boldsymbol{\phi}_t)) = R_t \begin{pmatrix} \omega_{t,2}h_3(r\boldsymbol{\phi}_t) - r\omega_{t,3}\phi_{t,2} \\ -\omega_{t,1}h_3(r\boldsymbol{\phi}_t) + r\omega_{t,3}\phi_{t,1} \\ r(\omega_{t,1}\phi_{t,2} - \omega_{t,2}\phi_{t,1}) \end{pmatrix}.$$

Inserting the expression (4.3) of $\boldsymbol{\omega}_t$ in cylindrical coordinates and using that, according to (2.5), $h_3(r\boldsymbol{\phi}_t) = \sqrt{k_0^2 - r^2} - k_0$, this becomes

$$\partial_t H(t, r\boldsymbol{\phi}_t) = \left(\rho_t \left(k_0 - \sqrt{k_0^2 - r^2}\right) + r\zeta_t\right) R_t \begin{pmatrix} -\phi_{t,2} \\ \phi_{t,1} \\ 0 \end{pmatrix}. \tag{B.1}$$

Denoting by DH the Jacobi matrix of H with respect to $\boldsymbol{k}$, we find with the chain rule

$$DH(t, r\boldsymbol{\phi}_t) \begin{pmatrix} -\phi_{t,2} \\ \phi_{t,1} \end{pmatrix} = R_t \begin{pmatrix} 1 & 0 \\ 0 & 1 \\ \frac{-r\phi_{t,1}}{\sqrt{k_0^2 - r^2}} & \frac{-r\phi_{t,2}}{\sqrt{k_0^2 - r^2}} \end{pmatrix} \begin{pmatrix} -\phi_{t,2} \\ \phi_{t,1} \end{pmatrix} = R_t \begin{pmatrix} -\phi_{t,2} \\ \phi_{t,1} \\ 0 \end{pmatrix}. \tag{B.2}$$

Comparing (B.1) and (B.2), we have that

$$\partial_t H(t, r\boldsymbol{\phi}_t) = \left(\rho_t \left(k_0 - \sqrt{k_0^2 - r^2}\right) + r\zeta_t\right) DH(t, r\boldsymbol{\phi}_t) \begin{pmatrix} -\phi_{t,2} \\ \phi_{t,1} \end{pmatrix}. \tag{B.3}$$

Recalling the definition $\nu_t(\boldsymbol{k}) = |\mathcal{F}[f](H(t, \boldsymbol{k}))|^2$, we have again by the chain rule

$$\begin{aligned} \partial_t \nu_t(\boldsymbol{k}) &= 2\,\mathrm{Re}\left(\mathcal{F}[f](H(t, \boldsymbol{k}))\right) \langle \nabla \mathcal{F}[f](H(t, \boldsymbol{k})), \partial_t H(t, \boldsymbol{k}) \rangle \quad \text{and} \\ \left\langle \nabla \nu_t(\boldsymbol{k}), \left(\begin{smallmatrix} -\phi_{t,2} \\ \phi_{t,1} \end{smallmatrix}\right) \right\rangle &= 2\,\mathrm{Re}\left(\mathcal{F}[f](H(t, \boldsymbol{k}))\right) \left\langle \nabla \mathcal{F}[f](H(t, \boldsymbol{k})), DH(t, \boldsymbol{k}) \left(\begin{smallmatrix} -\phi_{t,2} \\ \phi_{t,1} \end{smallmatrix}\right) \right\rangle, \end{aligned}$$

where $\nabla \mathcal{F}[f](\boldsymbol{y})$ denotes the gradient of $\mathcal{F}[f](\boldsymbol{y})$ with respect to $\boldsymbol{y} \in \mathbb{R}^3$. Inserting $\boldsymbol{k} = r\boldsymbol{\Phi}_t$ and using (B.3) yields the assertion. □

C Proofs of Section 5

Proof (of Lemma 5.1): (i) Since the elliptic arcs $\boldsymbol{\gamma}_{s,t}$ and $\boldsymbol{\gamma}_{t,s}$ have by construction the symmetry (3.10), we obtain for all $\beta \in J_{s,t}$ that

$$\begin{aligned} \mu_s(\boldsymbol{\gamma}_{s,t}(\beta)) &= \mathcal{F}[f]\left(R_s \boldsymbol{h}(\boldsymbol{\gamma}_{s,t}(\beta))\right) \mathrm{e}^{-\mathrm{i}\langle R_s \boldsymbol{d}_s, R_s \boldsymbol{h}(\boldsymbol{\gamma}_{s,t}(\beta))\rangle} \\ &= \mathcal{F}[f]\left(R_t \boldsymbol{h}(\boldsymbol{\gamma}_{t,s}(-\beta))\right) \mathrm{e}^{-\mathrm{i}\langle R_s \boldsymbol{d}_s, R_t \boldsymbol{h}(\boldsymbol{\gamma}_{t,s}(-\beta))\rangle} \\ &= \mu_t(\boldsymbol{\gamma}_{t,s}(-\beta))\, \mathrm{e}^{\mathrm{i}\langle R_t \boldsymbol{d}_t - R_s \boldsymbol{d}_s, R_t \boldsymbol{h}(\boldsymbol{\gamma}_{t,s}(-\beta))\rangle}, \end{aligned}$$

which implies (5.3) provided that $\mu_s(\boldsymbol{\gamma}_{s,t}(\beta))$ (or, equivalently, $\mu_t(\boldsymbol{\gamma}_{t,s}(-\beta))$) does not vanish.

(ii) In the same way, the elliptic arcs $\boldsymbol{\gamma}^*_{s,t}$ and $\boldsymbol{\gamma}^*_{t,s}$ have the symmetry (3.18). With the symmetry property (3.13) of $\mathcal{F}[f]$, we get for all $\beta \in J^*_{s,t}$ that

$$\begin{aligned} \mu_s(\boldsymbol{\gamma}^*_{s,t}(\beta)) &= \mathcal{F}[f]\left(R_s \boldsymbol{h}(\boldsymbol{\gamma}^*_{s,t}(\beta))\right) \mathrm{e}^{-\mathrm{i}\langle R_s \boldsymbol{d}_s, R_s \boldsymbol{h}(\boldsymbol{\gamma}^*_{s,t}(\beta))\rangle} \\ &= \mathcal{F}[f]\left(-R_t \boldsymbol{h}(\boldsymbol{\gamma}^*_{t,s}(\beta))\right) \mathrm{e}^{\mathrm{i}\langle R_s \boldsymbol{d}_s, R_t \boldsymbol{h}(\boldsymbol{\gamma}^*_{t,s}(\beta))\rangle} \\ &= \overline{\mu_t(\boldsymbol{\gamma}^*_{t,s}(\beta))}\, \mathrm{e}^{\mathrm{i}\langle R_s \boldsymbol{d}_s - R_t \boldsymbol{d}_t, R_t \boldsymbol{h}(\boldsymbol{\gamma}^*_{t,s}(\beta))\rangle}, \end{aligned}$$

which implies (5.4) provided that $\mu_s(\boldsymbol{\gamma}^*_{s,t}(\beta))$ (or, equivalently, $\mu_t(\boldsymbol{\gamma}^*_{t,s}(\beta))$) does not vanish. □

Proof (of Lemma 5.2): (i) If $R_t\boldsymbol{e}^3 = R_s\boldsymbol{e}^3$, we get for all $\boldsymbol{k} \in \mathcal{B}^2_{k_0}$, using that $R_s\boldsymbol{h}(\boldsymbol{k}) = R_t\boldsymbol{h}(\mathrm{Q}(-\alpha)\boldsymbol{k})$ according to (A.6),

$$\begin{aligned}\mu_t(\mathrm{Q}(-\alpha)\boldsymbol{k}) &= \mathcal{F}[f](R_t\boldsymbol{h}(\mathrm{Q}(-\alpha)\boldsymbol{k}))\mathrm{e}^{-\mathrm{i}\langle R_t\boldsymbol{d}_t, R_t\boldsymbol{h}(\mathrm{Q}(-\alpha)\boldsymbol{k})\rangle} \\ &= \mathcal{F}[f](R_s\boldsymbol{h}(\boldsymbol{k}))\mathrm{e}^{-\mathrm{i}\langle R_t\boldsymbol{d}_t, R_s\boldsymbol{h}(\boldsymbol{k})\rangle} = \mu_s(\boldsymbol{k})\mathrm{e}^{-\mathrm{i}\langle R_t\boldsymbol{d}_t - R_s\boldsymbol{d}_s, R_s\boldsymbol{h}(\boldsymbol{k})\rangle}.\end{aligned}$$

(ii) Similarly, we get for all $\boldsymbol{k} \in \mathcal{B}^2_{k_0}$ in the case $R_t\boldsymbol{e}^3 = -R_s\boldsymbol{e}^3$ with the corresponding relation $-R_s\boldsymbol{h}(\boldsymbol{k}) = R_t\boldsymbol{h}(\mathrm{Q}(-\alpha)\mathrm{S}\boldsymbol{k})$ from (A.7) that

$$\begin{aligned}\mu_t(\mathrm{Q}(-\alpha)\mathrm{S}\boldsymbol{k}) &= \mathcal{F}[f](R_t\boldsymbol{h}(\mathrm{Q}(-\alpha)\mathrm{S}\boldsymbol{k}))\mathrm{e}^{-\mathrm{i}\langle R_t\boldsymbol{d}_t, R_t\boldsymbol{h}(\mathrm{Q}(-\alpha)S\boldsymbol{k})\rangle} \\ &= \mathcal{F}[f](-R_s\boldsymbol{h}(\boldsymbol{k}))\mathrm{e}^{\mathrm{i}\langle R_t\boldsymbol{d}_t, R_s\boldsymbol{h}(\boldsymbol{k})\rangle} = \overline{\mu_s(\boldsymbol{k})}\mathrm{e}^{\mathrm{i}\langle R_t\boldsymbol{d}_t - R_s\boldsymbol{d}_s, R_s\boldsymbol{h}(\boldsymbol{k})\rangle}. \qquad \square\end{aligned}$$

Proof (of Theorem 5.3): (i) Since we know from our assumption of the scattering potential f being real-valued that

$$|\mu_s(\boldsymbol{0})| = |\mathcal{F}[f](\boldsymbol{0})| = (2\pi)^{-\frac{3}{2}}\int_{\mathbb{R}^3} f(\boldsymbol{x})\,\mathrm{d}\boldsymbol{x} > 0,$$

the equations (5.3) and (5.4) hold for all β in some open interval J around 0. By taking the logarithm of these equations, we find with the circular arcs $\boldsymbol{\sigma}_{s,t}$ and $\boldsymbol{\sigma}^*_{s,t}$, defined in (3.6) and (3.14), that

$$\langle R_t\boldsymbol{d}_t - R_s\boldsymbol{d}_s, \boldsymbol{\sigma}_{s,t}(\beta)\rangle = M(\beta) \quad \text{and} \tag{C.1}$$

$$\left\langle R_t\boldsymbol{d}_t - R_s\boldsymbol{d}_s, \boldsymbol{\sigma}^*_{s,t}(\beta)\right\rangle = M^*(\beta) \tag{C.2}$$

for all $\beta \in J$, where the functions $M\colon J \to \mathbb{C}$ and $M^*\colon J \to \mathbb{C}$, given by

$$M(\beta) \coloneqq -\mathrm{i}\int_0^\beta \frac{F'(\tilde\beta)}{F(\tilde\beta)}\,\mathrm{d}\tilde\beta, \quad F(\beta) \coloneqq \frac{\mu_s(\boldsymbol{\gamma}_{s,t}(\beta))}{\mu_t(\boldsymbol{\gamma}_{t,s}(-\beta))}, \quad \text{and}$$

$$M^*(\beta) \coloneqq -\mathrm{i}\int_0^\beta \frac{(F^*)'(\tilde\beta)}{F^*(\tilde\beta)}\,\mathrm{d}\tilde\beta, \quad F^*(\beta) \coloneqq \frac{\mu_s(\boldsymbol{\gamma}^*_{s,t}(\beta))}{\overline{\mu_t(\boldsymbol{\gamma}^*_{t,s}(\beta))}},$$

are explicitly known. Here, we used that the left-hand sides of (C.1) and (C.2) vanish for $\beta = 0$ to choose the correct branch of the logarithm of the continuously differentiable and nowhere vanishing functions F and F^*.

Inserting the expressions (3.6) and (3.14) for the circular arcs $\boldsymbol{\sigma}_{s,t}$ and $\boldsymbol{\sigma}^*_{s,t}$, respectively, we find, using the notation from Lemma 3.1 and Proposition 3.4, that we have for all $\beta \in J$ the equation system

$$\begin{aligned}a_{s,t}(\cos(\beta)-1)\left\langle R_s^\top R_t\boldsymbol{d}_t - \boldsymbol{d}_s, R_s^\top\boldsymbol{v}^1_{s,t}\right\rangle + a_{s,t}\sin(\beta)\left\langle R_s^\top R_t\boldsymbol{d}_t - \boldsymbol{d}_s, R_s^\top\boldsymbol{v}^2_{s,t}\right\rangle &= M(\beta), \\ a^*_{s,t}(\cos(\beta)-1)\left\langle R_s^\top R_t\boldsymbol{d}_t - \boldsymbol{d}_s, R_s^\top\boldsymbol{v}^3_{s,t}\right\rangle + a^*_{s,t}\sin(\beta)\left\langle R_s^\top R_t\boldsymbol{d}_t - \boldsymbol{d}_s, R_s^\top\boldsymbol{v}^2_{s,t}\right\rangle &= M^*(\beta).\end{aligned}$$

Since the functions $\beta \mapsto \cos(\beta) - 1$ and $\beta \mapsto \sin(\beta)$ are linearly independent on every interval with positive length, this implies that the coefficients

$$\left\langle R_s^\top R_t\boldsymbol{d}_t - \boldsymbol{d}_s, R_s^\top\boldsymbol{v}^j_{s,t}\right\rangle, \quad j \in \{1,2,3\},$$

are uniquely determined by this (recalling that we explicitly know the parameters $a_{s,t} \neq 0$ and $a^*_{s,t} \neq 0$). Since $(R_s^\top\boldsymbol{v}^j_{s,t})_{j=1}^3$ is an orthonormal basis of $\mathbb{R}^3$ (which we also know explicitly), this uniquely determines the vector $R_s^\top R_t\boldsymbol{d}_t - \boldsymbol{d}_s \in \mathbb{R}^3$.

(ii) Since $\mu_s(\mathbf{0}) \neq 0$, we find an open disk $A \subset \mathcal{B}^2_{k_0}$ that contains $\mathbf{0}$ such that we have $\mu_s(\boldsymbol{k}) \neq 0$ for all $\boldsymbol{k} \in A$. If $R_s^\top R_t \boldsymbol{e}^3 = \boldsymbol{e}^3$, we have that $R_s^\top R_t = Q^{(3)}(\alpha)$ for some $\alpha \in \mathbb{R}/(2\pi\mathbb{Z})$ and (5.5) implies

$$\left\langle R_s^\top R_t \boldsymbol{d}_t - \boldsymbol{d}_s, \boldsymbol{h}(\boldsymbol{k}) \right\rangle = -\mathrm{i} \int_{C_{\mathbf{0},\boldsymbol{k}}} \frac{\nabla G(\tilde{\boldsymbol{k}})}{G(\tilde{\boldsymbol{k}})} \,\mathrm{d}\tilde{\boldsymbol{k}} \quad \text{with} \quad G(\boldsymbol{k}) \coloneqq \frac{\mu_s(\boldsymbol{k})}{\mu_t(\mathrm{Q}(-\alpha)\boldsymbol{k})}$$

for all $\boldsymbol{k} \in A$, where $C_{\mathbf{0},\boldsymbol{k}}$ denotes an arbitrary curve from $\mathbf{0}$ to $\boldsymbol{k}$ in A. Since the vectors $\boldsymbol{h}(\boldsymbol{k})$ cover for $\boldsymbol{k} \in A$ an open subset of the hemisphere $\mathcal{H}_0$, they span all of $\mathbb{R}^3$, and thus this equation uniquely determines the vector $R_s^\top R_t \boldsymbol{d}_t - \boldsymbol{d}_s \in \mathbb{R}^3$.

Similarly, we have for $R_s^\top R_t \boldsymbol{e}^3 = -\boldsymbol{e}^3$ that $R_s^\top R_t = Q^{(2)}(\pi) Q^{(3)}(\alpha)$ for some $\alpha \in \mathbb{R}/(2\pi\mathbb{Z})$ and according to (5.6)

$$\left\langle R_s^\top R_t \boldsymbol{d}_t - \boldsymbol{d}_s, \boldsymbol{h}(\boldsymbol{k}) \right\rangle = -\mathrm{i} \int_{C_{\mathbf{0},\boldsymbol{k}}} \frac{\nabla G^*(\tilde{\boldsymbol{k}})}{G^*(\tilde{\boldsymbol{k}})} \,\mathrm{d}\tilde{\boldsymbol{k}} \quad \text{with} \quad G^*(\boldsymbol{k}) \coloneqq \frac{\mu_s(\boldsymbol{k})}{\mu_t(\mathrm{Q}(-\alpha) S \boldsymbol{k})}$$

for all $\boldsymbol{k} \in A$, which again uniquely determines $R_s^\top R_t \boldsymbol{d}_t - \boldsymbol{d}_s$. □

D Parameterization via Stereographic Projection

Based on the stereographic projection, we describe in this section a transformation that turns the elliptic arcs $\boldsymbol{\gamma}$, see (3.9), into straight lines in $\mathbb{R}^2$. Applying this transformation to the data ν_t, see (3.1), then one needs to detect common lines in the two-dimensional plane in order to reconstruct the rotation parameters. There are existing algorithms for detecting common lines in the context of motion detection the ray transform, cf. [35]. However, these lines all contain the origin, which is not the case for the diffraction tomography we consider here where we need an additional parameter to describe the lines.

D.1 Direct common circle method

We consider the stereographic projection $\boldsymbol{\pi}_t \colon \partial\mathcal{B}^3_{k_0}(-k_0 R_t \boldsymbol{e}^3) \setminus \{\mathbf{0}\} \to \mathcal{P}_t$ of the hemisphere $\mathcal{H}_t \setminus \{\mathbf{0}\}$ of the sphere $\partial\mathcal{B}^3_{k_0}(-k_0 R_t \boldsymbol{e}^3)$ from the origin onto the equatorial plane

$$\mathcal{P}_t \coloneqq \{\boldsymbol{x} \in \mathbb{R}^3 : \langle \boldsymbol{x}, R_t \boldsymbol{e}^3 \rangle = -k_0\}.$$

This maps every circle $\partial\mathcal{B}^3_{k_0}(-k_0 R_s \boldsymbol{e}^3) \cap \partial\mathcal{B}^3_{k_0}(-k_0 R_t \boldsymbol{e}^3)$ (as it passes through the origin, which could be defined to be mapped to infinity) to a straight line in $\mathcal{P}_t$.

The stereographic projection $\boldsymbol{\pi}_t$ of a point $\boldsymbol{x} \in \partial\mathcal{B}^3_{k_0}(-k_0 R_t \boldsymbol{e}^3) \setminus \{\mathbf{0}\}$ is hereby defined as the intersection of the line through $\mathbf{0}$ and $\boldsymbol{x}$ with the plane $\mathcal{P}_t$. In particular, we have for $t = 0$ where the rotation is $R_0 = I$ that $\boldsymbol{\pi}_0 \colon \partial\mathcal{B}^3_{k_0}(-k_0 \boldsymbol{e}^3) \setminus \{\mathbf{0}\} \to \mathcal{P}_0$

$$\boldsymbol{\pi}_0(\boldsymbol{x}) = \left(-k_0 \frac{x_1}{x_3}, -k_0 \frac{x_2}{x_3}, -k_0\right)^\top = -k_0 \frac{\boldsymbol{x}}{x_3}. \tag{D.1}$$

The stereographic projection $\boldsymbol{\pi}_t$ for general $t \in [0, T]$ is then obtained by rotating a point $\boldsymbol{x} \in \partial\mathcal{B}^3_{k_0}(-k_0 R_t \boldsymbol{e}^3)$ first to $\partial\mathcal{B}^3_{k_0}(-k_0 \boldsymbol{e}^3)$ and rotating the projected point in $\mathcal{P}_0$ back to $\mathcal{P}_t$, i.e.,

$$\boldsymbol{\pi}_t(\boldsymbol{x}) \coloneqq R_t \boldsymbol{\pi}_0(R_t^\top \boldsymbol{x}).$$

The following lemma shows that we can write all the projections $\boldsymbol{\pi}_t$ as restrictions of the function $\boldsymbol{\pi} \colon \mathbb{R}^3 \setminus \{\mathbf{0}\} \to \mathbb{R}^3 \setminus \{\mathbf{0}\}$ defined by

$$\boldsymbol{\pi}(\boldsymbol{x}) \coloneqq 2k_0^2 \frac{\boldsymbol{x}}{\|\boldsymbol{x}\|^2},$$

whose inverse is given by $\boldsymbol{\pi}^{-1} = \boldsymbol{\pi}$.

Lemma D.1 *For every $t \in [0,T]$, we have*

$$\boldsymbol{\pi}_t(\boldsymbol{x}) = \boldsymbol{\pi}(\boldsymbol{x}) \quad \textit{for all} \quad \boldsymbol{x} \in \partial\mathcal{B}^3_{k_0}(-k_0 R_t \boldsymbol{e}^3) \setminus \{\mathbf{0}\}.$$

Proof: Let $\boldsymbol{x} \in \partial\mathcal{B}^3_{k_0}(-k_0 R_t \boldsymbol{e}^3) \setminus \{\mathbf{0}\}$. Then we obtain

$$0 = \left\|\boldsymbol{x} + k_0 R_t \boldsymbol{e}^3\right\|^2 - k_0^2 = \|\boldsymbol{x}\|^2 + 2k_0 \langle R_t^\top \boldsymbol{x}, \boldsymbol{e}^3\rangle$$

and therefore

$$\boldsymbol{\pi}_t(\boldsymbol{x}) = R_t \boldsymbol{\pi}_0(R_t^\top \boldsymbol{x}) = -k_0 R_t \frac{R_t^\top \boldsymbol{x}}{\langle R_t^\top \boldsymbol{x}, \boldsymbol{e}^3\rangle} = 2k_0^2 \frac{\boldsymbol{x}}{\|\boldsymbol{x}\|^2} = \boldsymbol{\pi}(\boldsymbol{x}). \qquad \square$$

Next, we consider for arbitrary $t \in [0,T]$ the function $\tau\colon \mathcal{B}^2_{k_0} \setminus \{\mathbf{0}\} \to \mathbb{R}^2 \setminus \overline{\mathcal{B}^2_{k_0}}$ defined by

$$\tau(\boldsymbol{k}) \coloneqq P(R_t^\top \boldsymbol{\pi}_t(R_t \boldsymbol{h}(\boldsymbol{k}))) = P(\boldsymbol{\pi}_0(\boldsymbol{h}(\boldsymbol{k}))) = \frac{k_0}{k_0 - \kappa(\boldsymbol{k})}\boldsymbol{k}, \tag{D.2}$$

which describes the change from the parameterization via $R_t\boldsymbol{h}$ to the one via stereographic projection and is conveniently independent of the choice of $t \in [0,T]$. It maps by definition the data point $\boldsymbol{k}$ by the parameterization $R_t\boldsymbol{h}$ onto the hemisphere $\mathcal{H}_t$, stereographically projects it to $\mathcal{P}_t$ (with image $\mathcal{P}_t \setminus \overline{\mathcal{B}^3_{k_0}(-k_0 R_t \boldsymbol{e}^3)}$), and extracts the two components in the plane by rotating it to $\mathcal{P}_0$ and orthogonally projecting it with P to the first two components. Therefore it maps every elliptic arc $\boldsymbol{\gamma}_{t,s}$ to a straight line. The codomain of τ is chosen so that τ is bijective, and its inverse is given by

$$\tau^{-1}(\boldsymbol{y}) = \frac{2k_0^2}{k_0^2 + \|\boldsymbol{y}\|^2}\boldsymbol{y}, \quad \boldsymbol{y} \in \mathbb{R}^2 \setminus \overline{\mathcal{B}^2_{k_0}}.$$

Lemma D.2 *Let $s,t \in [0,T]$ such that $R_s\boldsymbol{e}^3 \neq \pm R_t\boldsymbol{e}^3$ and $(\varphi,\theta,\psi) \in (\mathbb{R}/(2\pi\mathbb{Z})) \times [0,\pi] \times (\mathbb{R}/(2\pi\mathbb{Z}))$ be the Euler angles of the rotation $R_s^\top R_t$ as in (3.11).*

(i) The elliptic arc $\boldsymbol{\gamma}_{s,t}$ defined in (3.9) fulfills

$$\tau(\boldsymbol{\gamma}_{s,t}(\beta)) = -k_0 \tan(\tfrac{\theta}{2}) \begin{pmatrix}\cos(\varphi)\\ \sin(\varphi)\end{pmatrix} + \frac{k_0}{\cos(\frac{\theta}{2})} \cot(\tfrac{\beta}{2}) \begin{pmatrix}-\sin(\varphi)\\ \cos(\varphi)\end{pmatrix}, \quad \beta \in J_{s,t} \setminus \{0\}. \tag{D.3}$$

(ii) The dual elliptic arc $\boldsymbol{\gamma}^*_{s,t}$ given by (3.16) fulfills

$$\tau(\boldsymbol{\gamma}^*_{s,t}(\beta)) = k_0 \cot(\tfrac{\theta}{2}) \begin{pmatrix}\cos(\varphi)\\ \sin(\varphi)\end{pmatrix} - \frac{k_0}{\sin(\frac{\theta}{2})} \cot(\tfrac{\beta}{2}) \begin{pmatrix}-\sin(\varphi)\\ \cos(\varphi)\end{pmatrix}, \quad \beta \in J^*_{s,t} \setminus \{0\}. \tag{D.4}$$

Proof: (i) We use (3.8) to write

$$\tau(\boldsymbol{\gamma}_{s,t}(\beta)) = P(\boldsymbol{\pi}_0(\boldsymbol{h}(\boldsymbol{\gamma}_{s,t}(\beta)))) = P(\boldsymbol{\pi}_0(R_s^\top \boldsymbol{\sigma}_{s,t}(\beta))).$$

Plugging in the expression (3.6) for the circular arc $\boldsymbol{\sigma}_{s,t}$ and the definition (D.1) of the function $\boldsymbol{\pi}_0$, we arrive at

$$\tau(\boldsymbol{\gamma}_{s,t}(\beta)) = k_0 \frac{a_{s,t}(\cos(\beta)-1)P(R_s^\top \boldsymbol{v}^1_{s,t}) + a_{s,t}\sin(\beta)P(R_s^\top \boldsymbol{v}^2_{s,t})}{\frac{k_0}{2}(1-\cos(\beta))(1+\langle R_s\boldsymbol{e}^3, R_t\boldsymbol{e}^3\rangle)}.$$

As in Lemma 3.2, where we already calculated the projections of the basis vectors $\boldsymbol{v}^1_{s,t}$ and $\boldsymbol{v}^2_{s,t}$ in (A.4), we can rewrite this in the form

$$\tau(\boldsymbol{\gamma}_{s,t}(\beta)) = 2\frac{\tilde{a}_{s,t}(\cos(\beta)-1)\boldsymbol{w}^1_{s,t} + a_{s,t}\sin(\beta)\boldsymbol{w}^2_{s,t}}{(1-\cos(\beta))(1+\langle R_s\boldsymbol{e}^3, R_t\boldsymbol{e}^3\rangle)}.$$

Using $1+\langle R_s\boldsymbol{e}^3, R_t\boldsymbol{e}^3\rangle = \frac{1}{2}\left\|R_s\boldsymbol{e}^3 + R_t\boldsymbol{e}^3\right\|^2 = \frac{2}{k_0^2}a^2_{s,t}$ and the trigonometric identity $\frac{\sin(\beta)}{1-\cos(\beta)} = \cot(\frac{\beta}{2})$, this becomes

$$\tau(\boldsymbol{\gamma}_{s,t}(\beta)) = -\frac{k_0^2\tilde{a}_{s,t}}{a^2_{s,t}}\boldsymbol{w}^1_{s,t} + \frac{k_0^2}{a_{s,t}}\cot(\tfrac{\beta}{2})\boldsymbol{w}^2_{s,t}.$$

Inserting the expressions for the parameters in Euler angles as in Proposition 3.3, we obtain (D.3).

(ii) In the same way, we find with the results and the notation of Proposition 3.4 that

$$\tau(\boldsymbol{\gamma}^*_{s,t}(\beta)) = P(\boldsymbol{\pi}_0(R_s^\top\boldsymbol{\sigma}^*_{s,t}(\beta))) = -k_0\frac{a^*_{s,t}(\cos(\beta)-1)P(R_s^\top\boldsymbol{v}^3_{s,t}) - a^*_{s,t}\sin(\beta)P(R_s^\top\boldsymbol{v}^2_{s,t})}{\frac{k_0}{2}(\cos(\beta)-1)(1-\langle R_s\boldsymbol{e}^3, R_t\boldsymbol{e}^3\rangle)}.$$

Using (A.4) and (A.5) to express the projections of the basis vectors $\boldsymbol{v}^2_{s,t}$ and $\boldsymbol{v}^3_{s,t}$, we get with $1-\langle R_s\boldsymbol{e}^3, R_t\boldsymbol{e}^3\rangle = \frac{1}{2}\left\|R_s\boldsymbol{e}^3 - R_t\boldsymbol{e}^3\right\|^2 = \frac{2}{k_0^2}(a^*_{s,t})^2$ that

$$\tau(\boldsymbol{\gamma}^*_{s,t}(\beta)) = k_0^2\frac{\tilde{a}_{s,t}}{(a^*_{s,t})^2}\boldsymbol{w}^1_{s,t} - \frac{k_0^2}{a^*_{s,t}}\cot(\tfrac{\beta}{2})\boldsymbol{w}^2_{s,t}.$$

Inserting the expressions for the parameters in Euler angles as in Proposition 3.3 and Proposition 3.4, this becomes (D.4). □

From the definitions of the intervals $J_{s,t}$ and $J^*_{s,t}$, the functions $\tau\circ\boldsymbol{\gamma}_{s,t}\colon J_{s,t}\setminus\{0\}\to\mathbb{R}^2\setminus\overline{\mathcal{B}^2_{k_0}}$ from (D.3) and $\tau\circ\boldsymbol{\gamma}^*_{s,t}\colon J^*_{s,t}\setminus\{0\}\to\mathbb{R}^2\setminus\overline{\mathcal{B}^2_{k_0}}$ from (D.4) parameterize the parts of straight lines in $\mathbb{R}^2$ which are outside the ball $\overline{\mathcal{B}^2_{k_0}}$, see Figure 13.

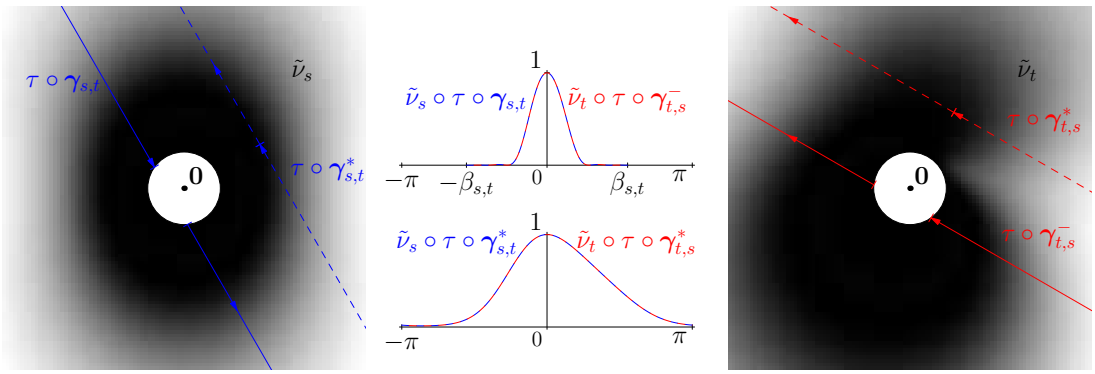

Figure 13: Transformed scaled squared energies $\tilde{\nu}_s$ and $\tilde{\nu}_t$, see (D.5), for the same situation as in Figure 5 and the paths of the corresponding two straight lines $\tau\circ\boldsymbol{\gamma}_{s,t}$ and $\tau\circ\boldsymbol{\gamma}^-_{t,s}$ (the minus again indicating the reversed direction) and their dual straight lines $\tau\circ\boldsymbol{\gamma}^*_{s,t}$ and $\tau\circ\boldsymbol{\gamma}^*_{t,s}$. The values of $\tilde{\nu}_s$ and $\tilde{\nu}_t$ along the lines are plotted in the center of the figure.

Thus, looking for straight lines in the *transformed scaled squared energy* $\tilde{\nu}_t\colon\mathbb{R}^2\setminus\overline{\mathcal{B}^2_{k_0}}\to[0,\infty)$, defined by

$$\tilde{\nu}_t := \nu_t\circ\tau^{-1} \quad \text{for all} \quad t\in[0,T], \tag{D.5}$$

we can recover the Euler angles as in Theorem 3.6. This is summarized in the following theorem.

Theorem D.3 *Let $s,t\in[0,T]$ such that $R_s\boldsymbol{e}^3\neq\pm R_t\boldsymbol{e}^3$ and assume that there uniquely exist two pairs $(\boldsymbol{\Gamma}_\ell)_{\ell=1}^2$ and $(\boldsymbol{\Gamma}_\ell^*)_{\ell=1}^2$ of straight lines of the form*

$$\boldsymbol{\Gamma}_\ell\colon\mathbb{R}\to\mathbb{R}^2,\quad \boldsymbol{\Gamma}_\ell(\xi)\coloneqq -b\boldsymbol{w}_\ell^1+\xi\boldsymbol{w}_\ell^2,\quad \text{and} \tag{D.6}$$

$$\boldsymbol{\Gamma}_\ell^*\colon\mathbb{R}\to\mathbb{R}^2,\quad \boldsymbol{\Gamma}^*{}_\ell(\xi)\coloneqq \frac{k_0^2}{b}\boldsymbol{w}_\ell^1-\xi\boldsymbol{w}_\ell^2,\quad \ell\in\{1,2\}, \tag{D.7}$$

for some parameter $b\in(0,\infty)$ and two positively oriented, orthonormal bases $(\boldsymbol{w}_1^j)_{j=1}^2$ and $(\boldsymbol{w}_2^j)_{j=1}^2$ of $\mathbb{R}^2$ such that we have for the transformed scaled squared energy $\tilde{\nu}_t$ that

$$\begin{aligned}\tilde{\nu}_s(\boldsymbol{\Gamma}_1(\xi))&=\tilde{\nu}_t(\boldsymbol{\Gamma}_2(-\xi))\quad \text{for all}\quad \xi\in\mathbb{R}\quad \text{with}\quad \xi^2>k_0^2-b^2,\\ \tilde{\nu}_s(\boldsymbol{\Gamma}_1^*(\xi))&=\tilde{\nu}_t(\boldsymbol{\Gamma}_2^*(\xi))\quad \text{for all}\quad \xi\in\mathbb{R}\quad \text{with}\quad \xi^2>k_0^2-k_0^4b^{-2}.\end{aligned}$$

Then the relative rotation is given by

$$R_s^\top R_t=Q^{(3)}(\arg(\boldsymbol{w}_1^1))Q^{(2)}(2\arctan(\tfrac{b}{k_0}))Q^{(3)}(\pi-\arg(\boldsymbol{w}_2^1)). \tag{D.8}$$

Proof: We parameterize $R_s^\top R_t$ in Euler angles $(\varphi,\theta,\psi)\in(\mathbb{R}/(2\pi\mathbb{Z}))\times[0,\pi]\times(\mathbb{R}/(2\pi\mathbb{Z}))$ as in (3.11) and get for the representation of $R_t^\top R_s$ in Euler angles the formula (A.8). Then, we consider the straight lines $\tau\circ\boldsymbol{\gamma}_{s,t}$ and $\tau\circ\boldsymbol{\gamma}_{s,t}^*$, given by (D.3) and (D.4), where $\boldsymbol{\gamma}_{s,t}$ and $\boldsymbol{\gamma}_{s,t}^*$ denote the elliptic arcs introduced in (3.9) and (3.16), and reparameterize them via the functions

$$\begin{aligned}\Xi\colon J_{s,t}\setminus\{0\}&\to\{\xi\in\mathbb{R}:\xi^2>k_0^2-k_0^2\tan^2(\tfrac{\theta}{2})\},\quad \Xi(\beta)\coloneqq\frac{k_0}{\cos(\frac{\theta}{2})}\cot(\tfrac{\beta}{2}),\quad \text{and}\\ \Xi^*\colon J_{s,t}^*\setminus\{0\}&\to\{\xi\in\mathbb{R}:\xi^2>k_0^2-k_0^2\cot^2(\tfrac{\theta}{2})\},\quad \Xi^*(\beta)\coloneqq\frac{k_0}{\sin(\frac{\theta}{2})}\cot(\tfrac{\beta}{2}),\end{aligned}$$

which are seen to be bijective by using that $\beta\in J_{s,t}$ is by definition (3.7) for $\beta\in(-\pi,\pi]$ equivalent to $\cos(\beta)>\frac{\cos(\theta)-1}{\cos(\theta)+1}$, which is equivalent to $\cot^2(\frac{\beta}{2})=\frac{1+\cos(\beta)}{1-\cos(\beta)}>\cos(\theta)$, and therefore to

$$(\Xi(\beta))^2+k_0^2\tan^2(\tfrac{\theta}{2})>\frac{k_0^2}{\cos^2(\frac{\theta}{2})}(\cos^2(\tfrac{\theta}{2})-\sin^2(\tfrac{\theta}{2}))+k_0^2\tan^2(\tfrac{\theta}{2})=k_0^2.$$

Analogously, we find that $\beta\in J_{s,t}^*$ is by definition (3.15) for $\beta\in(-\pi,\pi]$ equivalent to $\cos(\beta)>\frac{\cos(\theta)+1}{\cos(\theta)-1}$, which is equivalent to $\cot^2(\frac{\beta}{2})=\frac{1+\cos(\beta)}{1-\cos(\beta)}>-\cos(\theta)$, and therefore to

$$(\Xi^*(\beta))^2+k_0^2\cot^2(\tfrac{\theta}{2})>\frac{k_0^2}{\sin^2(\frac{\theta}{2})}(\sin^2(\tfrac{\theta}{2})-\cos^2(\tfrac{\theta}{2}))+k_0^2\cot^2(\tfrac{\theta}{2})=k_0^2.$$

Then, according to (D.3), the curves $\tau\circ\boldsymbol{\gamma}_{s,t}\circ\Xi^{-1}$ and $\tau\circ\boldsymbol{\gamma}_{t,s}\circ\Xi^{-1}$ are with

$$b=k_0\tan(\tfrac{\theta}{2}),\quad \boldsymbol{w}_1^1=\boldsymbol{w}_{s,t}^1=\begin{pmatrix}\cos(\varphi)\\ \sin(\varphi)\end{pmatrix},\quad \text{and}\quad \boldsymbol{w}_2^1=\boldsymbol{w}_{t,s}^1=\begin{pmatrix}\cos(\pi-\psi)\\ \sin(\pi-\psi)\end{pmatrix} \tag{D.9}$$

on the set $X\coloneqq\{\xi\in\mathbb{R}:\xi^2>k_0^2-b^2\}$ of the form (D.6); and according to (D.4), the dual curves $\tau\circ\boldsymbol{\gamma}_{s,t}^*\circ(\Xi^*)^{-1}$ and $\tau\circ\boldsymbol{\gamma}_{t,s}^*\circ(\Xi^*)^{-1}$ are with this on the set $X^*\coloneqq\{\xi\in\mathbb{R}:\xi^2>k_0^2-k_0^4b^{-2}\}$ of the form (D.7). Moreover, these curves fulfill according to (3.10) and (3.18) the relations

$$\begin{aligned}\tilde{\nu}_s(\tau(\boldsymbol{\gamma}_{s,t}(\Xi^{-1}(\xi))))&=\nu_s(\boldsymbol{\gamma}_{s,t}(\Xi^{-1}(\xi)))\\ &=\nu_t(\boldsymbol{\gamma}_{t,s}(-\Xi^{-1}(\xi)))=\tilde{\nu}_t(\tau(\boldsymbol{\gamma}_{t,s}(\Xi^{-1}(-\xi)))),\quad \xi\in X,\\ \tilde{\nu}_s(\tau(\boldsymbol{\gamma}_{s,t}^*((\Xi^*)^{-1}(\xi))))&=\nu_s(\boldsymbol{\gamma}_{s,t}^*((\Xi^*)^{-1}(\xi)))\\ &=\nu_t(\boldsymbol{\gamma}_{t,s}^*((\Xi^*)^{-1}(\xi)))=\tilde{\nu}_t(\tau(\boldsymbol{\gamma}_{t,s}^*((\Xi^*)^{-1}(\xi)))),\quad \xi\in X^*.\end{aligned}$$

The uniqueness of the pairs $(\boldsymbol{\Gamma}_\ell)_{\ell=1}^2$ and $(\boldsymbol{\Gamma}_\ell^*)_{\ell=1}^2$ therefore implies $\boldsymbol{\Gamma}_1=\tau\circ\boldsymbol{\gamma}_{s,t}\circ\Xi^{-1}$, $\boldsymbol{\Gamma}_2=\tau\circ\boldsymbol{\gamma}_{t,s}\circ\Xi^{-1}$, $\boldsymbol{\Gamma}_1^*=\tau\circ\boldsymbol{\gamma}_{s,t}^*\circ(\Xi^*)^{-1}$, and $\boldsymbol{\Gamma}_2^*=\tau\circ\boldsymbol{\gamma}_{t,s}^*\circ(\Xi^*)^{-1}$, so that we can read off the Euler angles from the correspondencies (D.9), giving us the reconstruction (D.8). □

D.2 Infinitesimal common circle method

We can also formulate the infinitesimal common circle method from Section 4 via common lines. We show the following analogue of Lemma 4.1, where the coefficient of the spatial derivative becomes affine.

Lemma D.4 *Let the rotations $R \in C^1([0,T] \to \mathrm{SO}(3))$ be continuously differentiable and the associated angular velocities $\boldsymbol{\omega}_t \in \mathbb{R}^3$ be written in cylindrical coordinates (4.3). Then, the transformed scaled squared energy $\tilde{\nu}_t$, defined in (D.5), satisfies for every $r \in \mathbb{R} \setminus [-k_0, k_0]$ and $t \in [0,T]$ the relation*

$$\partial_t \tilde{\nu}_t(r\boldsymbol{\phi}_t) = (k_0\rho_t + r\zeta_t)\left\langle \nabla \tilde{\nu}_t(r\boldsymbol{\phi}_t), \begin{pmatrix} -\phi_{t,2} \\ \phi_{t,1} \end{pmatrix} \right\rangle. \tag{D.10}$$

Proof: The transformed data $\tilde{\nu}_t$ is given by

$$\tilde{\nu}_t(\boldsymbol{y}) = \nu_t(\tau^{-1}(\boldsymbol{y})) = \left|\mathcal{F}[f](R_t \boldsymbol{h}(\tau^{-1}(\boldsymbol{y})))\right|^2.$$

Using now that we have by definition (D.1) of $\boldsymbol{\pi}_0$ and definition (D.2) of τ that

$$\begin{pmatrix} \tau(\tau^{-1}(\boldsymbol{y})) \\ -k_0 \end{pmatrix} = \boldsymbol{\pi}_0(\boldsymbol{h}(\tau^{-1}(\boldsymbol{y}))) = R_t^\top \boldsymbol{\pi}_t(R_t \boldsymbol{h}(\tau^{-1}(\boldsymbol{y}))),$$

we have with Lemma D.1 and $\boldsymbol{\pi}^{-1} = \boldsymbol{\pi}$ the relation

$$\tilde{\nu}_t(\boldsymbol{y}) = \left|\mathcal{F}[f](R_t \boldsymbol{h}(\tau^{-1}(\boldsymbol{y})))\right|^2 = \left|\mathcal{F}[f](\boldsymbol{\pi}((t,\boldsymbol{y})))\right|^2 \tag{D.11}$$

with the function $K\colon [0,T] \times \mathbb{R}^2 \setminus \overline{\mathcal{B}_{k_0}^2} \to \mathbb{R}^3$ defined by $K(t,\boldsymbol{y}) \coloneqq R_t \begin{pmatrix} \boldsymbol{y} \\ -k_0 \end{pmatrix}$.

Since the partial derivative $\partial_t K$ of K with respect to t fulfills

$$\partial_t K(t, r\boldsymbol{\phi}_t) = R_t\left(\omega_t \times \begin{pmatrix} r\boldsymbol{\phi}_t \\ -k_0 \end{pmatrix}\right) = R_t\left(\begin{pmatrix} \rho_t \boldsymbol{\phi}_t \\ \zeta_t \end{pmatrix} \times \begin{pmatrix} r\boldsymbol{\phi}_t \\ -k_0 \end{pmatrix}\right) = (k_0\rho_t + r\zeta_t) R_t \begin{pmatrix} -\phi_{t,2} \\ \phi_{t,1} \\ 0 \end{pmatrix}$$

and the Jacobi matrix DK of K with respect to $\boldsymbol{y}$ satisfies

$$DK(t, r\boldsymbol{\phi}_t)\begin{pmatrix} -\phi_{t,2} \\ \phi_{t,1} \end{pmatrix} = R_t \begin{pmatrix} 1 & 0 \\ 0 & 1 \\ 0 & 0 \end{pmatrix} \begin{pmatrix} -\phi_{t,2} \\ \phi_{t,1} \end{pmatrix} = R_t \begin{pmatrix} -\phi_{t,2} \\ \phi_{t,1} \\ 0 \end{pmatrix},$$

we have

$$\partial_t K(t, r\boldsymbol{\phi}_t) = (k_0\rho_t + r\zeta_t) DK(t, r\boldsymbol{\phi}_t)\begin{pmatrix} -\phi_{t,2} \\ \phi_{t,1} \end{pmatrix},$$

which implies with (D.11) directly (D.10). □

We obtain the following analogue to Theorem 4.2 for reconstructing the angular velocity $\boldsymbol{\omega}_t$, from which we can determine the rotation matrices R_t by Theorem 4.3.

Theorem D.5 *Let the rotations $R \in C^1([0,T] \to \mathrm{SO}(3))$ be continuously differentiable and $t \in [0,T]$. Let further $\boldsymbol{\phi} \in \mathbb{S}^1_+$ be a unique direction with the property that there exist parameters $\rho, \zeta \in \mathbb{R}$ with*

$$\partial_t \tilde{\nu}_t(r\boldsymbol{\phi}) = (k_0\rho + r\zeta)\left\langle \nabla \tilde{\nu}_t(r\boldsymbol{\phi}), \begin{pmatrix} -\phi_2 \\ \phi_1 \end{pmatrix} \right\rangle \quad \text{for all} \quad r \in \mathbb{R} \setminus [-k_0, k_0]$$

for the transformed scaled squared energy $\tilde{\nu}_t$ in (D.5). Provided that the set

$$\mathcal{M}_t \coloneqq \left\{ r \in \mathbb{R} \setminus [-k_0, k_0] : \left\langle \nabla \tilde{\nu}_t(r\boldsymbol{\phi}), \begin{pmatrix} -\phi_2 \\ \phi_1 \end{pmatrix} \right\rangle \neq 0 \right\}$$

contains at least two elements, then the angular velocity is given by $\boldsymbol{\omega}_t = (\rho\boldsymbol{\phi}, \zeta)^\top$.

Proof: From Lemma D.4, we find that the uniqueness implies that $\boldsymbol{\phi}_t = \boldsymbol{\phi}$ and therefore also

$$k_0\rho + r\zeta = k_0\rho_t + r\zeta_t \quad \text{for all} \quad r \in \mathcal{M}_t.$$

Hence we have $\rho = \rho_t$ and $\zeta = \zeta_t$ if the equation is satisfied for two different values r. □